A theoretical and experimental investigation on the effect that slow heating and cooling has on the inter-diffusion parameters of Cu/Ni thin films.

by

Heinrich Daniel Joubert

M.Sc.

a thesis presented in fulfilment of the requirements of the degree

Philosophiæ Doctor

in the Department of Physics

at the University of the Free State

Republic of South Africa

Promoter: **Prof J.J. Terblans**

Co-promoter: **Prof H.C. Swart**

May 2010

For

My wife

Elizma

And

My parents

Anton & Sophie

Acknowledgements

The author wishes to express his thanks and gratitude to the following people:

- *My parents*, for their unending love and support. Without you none of this would have been possible
- *Elizma,* for her understanding, motivation and love
- *My promoters*, for all their patience, support and friendship through all the years of this study
- *The National Research Foundation*, for financial assistance
- *The personnel of the Physics Department of the University of the Free State*, for numerous informative conversations
- *Mr Adriaan Hugo and Mr Innes Basson,* for their electronics know-how and speedy repairs of the control units of the SAM 590
- *Mr Shaun Cronjé,* for all his help and support with loading of samples and repairing the SAM
- *The Lord God,* for giving me strength to carry on during difficult times

Key words

Diffusion

Activation energy

Depth profiling

Linear least squares

Shimizu

Matrix factors

Thin films

Linear temperature ramping

Mixing-Roughness-Information (MRI) model

Depth resolution function

Auger electron spectroscopy

Ni

Cu

Abstract

Thin film diffusion studies often involve a surface sensitive analysis technique combined with ion erosion to produce a depth profile of a sample. Such studies compare the depth profile of a reference sample to the depth profiles of samples that were annealed at different temperatures and times. The extent to which atoms of one layer diffuse into an adjacent layer, for a particular temperature and time, yields information on the diffusion process involved and allows quantification of the diffusion coefficient. The drawback to using an erosion type system is the effect of the incident ions on the surface being probed. The Mixing-Roughness-Information model attempts to compensate for this effect and is often employed as a means of quantification of measured depth profiles by means of profile reconstruction. Used in conjunction with Auger electron spectroscopy, the Mixing-Roughness-Information (MRI) model is a useful tool to reconstruct the ion erosion depth profiles as well as extracting inter-diffusion parameters from these depth profiles. The first part of the study focuses on the extraction of the diffusion coefficient of classically annealed samples of Ni in Cu from Ni/Cu depth profiles obtained from ion erosion Auger electron spectroscopy. The resultant depth profiles were reconstructed with the MRI model. The diffusion coefficient for Ni diffusing in Cu was obtained from the MRI fit and it compared well to values available in literature. From an Arrhenius graph a value of $D_0 = 6.49 \times 10^{-9}$ $m^2.s^{-1}$ for the pre-exponential factor and $Q = 130.5$ $kJ.mol^{-1}$ for the activation energy was calculated.

The second part of the study involves linear ramping as an annealing technique. In previous studies, linear temperature ramping was used to determine diffusion

coefficients from bulk-to-surface segregation experiments of a low concentration solute. Thin film diffusion studies usually employ a classical heating regime, where a sample's annealing time is taken as the time between insertion and removal from a furnace. The aforementioned study type assumes that the time it takes to heat a sample after insertion is instantaneous, while the sample cools down instantaneously after removal from the furnace. This assumption is incorrect, as it does not compensate for the various mechanisms that govern heat transfer. In order to eliminate the uncertainty, a linear ramping regime is used and samples were annealed inside an UHV environment with a programmed linear heating scheme. After each anneal, a depth profile was obtained by simultaneously bombarding the sample with Ar^+ ions and monitoring the exposed surface with an electron beam which excites Auger electrons, among others. The depth profiles were normalised and the time scale converted to depth. In order to compare the diffusion profiles obtained from classical annealing studies to the linearly ramped studies, the diffusion coefficient obtained for a classical study of Ni diffusing in Cu was compared to the diffusion coefficient obtained from a MRI linear ramp analysis of the ramped samples. The linear ramp analysis yielded a pre-exponential factor of $D_0 = 2.29 \times 10^{-13}$ $m^2.s^{-1}$ and activation energy of $Q = 82.5$ $kJ.mol^{-1}$. Comparison of the diffusion profiles calculated with the diffusion coefficients obtained from classical heating and linear heating showed a large discrepancy between the calculated diffusion profiles. Analysis of the calculated profiles showed that classical diffusion studies over-estimate the rate of diffusion if compared to the diffusion profile calculated with diffusion parameters obtained from linear ramping experiments.

The linear ramping MRI technique was extended even further by changing the heating and cooling rate, thereby decreasing the effective annealing time. Diffusion profiles obtained from the extended linear heating MRI method refined the diffusion parameters for linear ramping even further.

Table of Contents

Chapter 1 - Introduction

Diffusion is one of the basic concepts of nature that is easy to observe. Almost everyone has experienced diffusion in some form or another, whether consciously or not. A simple way to demonstrate diffusion is by adding a drop of ink or dye to a glass of water. The ink/dye will slowly spread through the glass until the concentration of the ink/dye in the glass is uniform. This above example explores a concept that is very important in diffusion, namely equilibrium conditions and concentration gradients.

The concentration gradient between the water in the glass and the drop of ink causes the ink to *diffuse* through the water and demonstrates the concept of minimization of energy, where any material that is not in thermodynamic equilibrium will tend to reorganize itself at the atomic level so that equilibrium is attained [1]. Diffusion attempts to eliminate any unstable energy situations that occur when the free energy of a microscopic system varies from one position to another. This difference in energy might be a result of differences in the concentration gradient of a substance which in turn results in mass transport that will reduce the concentration gradient and eventually eliminate it.

Naturally, diffusion is not limited to liquid solutions only. Diffusion also occurs in other systems and over the past 50 years diffusion in metals has received significant attention in the scientific community. Diffusion is a very important factor in the design of materials for both physicists and metallurgists [2]. It is important to

metallurgists since phenomena such as the carburisation of steel, production of corrosion/heat resisting substances and other properties all depend on diffusion rates [2]. Physicists are interested in diffusion as it throws light on the mechanism of rate processes in solids as it involves atomic movements [2].

Most diffusion studies are carried out by annealing a sample for a certain time at a certain temperature. This process causes diffusion, which changes the composition of the sample. If one can then determine the composition of the sample, the diffusion coefficient can be determined. Once the diffusion coefficient is known, scientists and engineers can predict what the composition of a sample will be if it is annealed at a different temperature and time, allowing for the creation of materials that have very specific engineering properties, as discussed in the previous paragraph.

Producing a sample with a predicted composition relies heavily on the annealing temperature as well as the annealing time. If these two parameters are not carefully controlled, the resultant composition of the material will differ from the desired composition. The annealing temperature and time is the subject of this study and a detailed investigation into the effects that the annealing method has on the sample composition was carried out. Included in the annealing method investigation is an investigation into the diffusion process, which yielded enough information to proceed to an experimental study.

The experimental study attempted to compare the classical method of annealing to a new controlled method of annealing. The controlled method of annealing eliminates all the unknown factors that contribute to a sample heating up and cooling down,

thereby carefully controlling the amount of energy transferred to a sample during the annealing process. By controlling the annealing method, the diffusion process can also be controlled to a higher level, allowing for the creation of samples with a well-defined composition.

1.1 Layout of the thesis

Chapter 2 introduces the reader to the concept of diffusion and analyses the diffusion process in detail. The diffusion equation is analysed and an expression for the pre-exponential frequency factor and activation energy is derived for self-diffusion. Inter-diffusion is also discussed in this chapter.

Chapter 3 covers depth profiling and depth profile reconstruction. The depth resolution function is defined and the Mixing-Roughness-Information model is discussed.

Chapter 4 analyses the process of annealing by incorporating the various methods of heat transfer into a numerical solution of Fick's second law. A comparison is then made between a sample annealed using the classical error function solution and a numerical solution of Fick's second law, with the results indicating a large difference between the two types of calculation methods.

Chapter 5 discusses the experimental setup used in this study, as well as techniques that can be used to analyse Auger spectrums and depth profiles obtained from Auger

electron spectroscopy. There is also a short section on the Mixing-Roughness-Information model software that was written for this study.

Chapter 6 is concerned with the results of the experimental part of the study, dividing the results into a classical annealing section and a linear ramping annealing section. A comparison is made between diffusion parameters obtained from the classical analysis and linear ramping analysis. The effect that changing the linear ramping rate has on the measured diffusion profiles is also discussed.

Chapter 7 provides a brief conclusion.

Chapter 2 – Diffusion Theory

2.1 Introduction

All the possible applications that involve diffusion share one common factor: minimizing of the local energy to obtain equilibrium. The first person to describe diffusion in any amount of detail was Adolf Eugene Fick who derived the now famous Fick's diffusion laws in 1855 [3]. This chapter will mention the two laws of Fick and apply these equations to the two types of diffusion that have been observed: self-diffusion and inter-diffusion. Self-diffusion covers atomic movements in a system that contains only one element, while inter-diffusion covers atomic movements in systems that contain two or more elements.

2.2 The laws of Fick

Changes in the atomic concentration in a solid can only be achieved through diffusion, which in turn implies that there must be a relation between atomic motion and concentration. This relationship is described by a property known as the diffusion coefficient. Fick's first law describes the diffusion coefficient in terms of the jump frequency and jump distance of the atoms.

If one considers a crystal where all the diffusing atoms are of the same element, i.e. self-diffusion, the diffusion coefficient (D) will be independent of the concentration of

the crystal [4]. If an atom jumps Γ times per second and the total distance that it moves is given by Δx, the total flux of atoms is given by

$$J = -\frac{1}{2}\Gamma(\Delta x)^2 \frac{\partial C}{\partial x} = -D\frac{\partial C}{\partial x} \tag{2.1}$$

with the diffusion coefficient given by $D = \frac{1}{2}\Gamma(\Delta x)^2$ and C the concentration. Equation (2.1) is Fick's first law [4, 5], derived for a one-dimensional setup. The factor $\frac{1}{2}$ indicates diffusion in one dimension. If the derivation was done for a 3-dimensional setup, the diffusion coefficient will be [6]

$$D = \frac{1}{6}\Gamma(\Delta x)^2. \tag{2.2}$$

In most practical situations steady-state conditions are not established. The concentration varies with both distance and time, and Fick's first law can no longer be used. In such instances, Fick's second law is used to determine how the concentration of atoms at any point in a material varies with time, given by [7]

$$\frac{\partial C}{\partial t} = D\frac{\partial^2 C}{\partial x^2}, \tag{2.3}$$

where C is the concentration, t is time and x is the position in the crystal. A full derivation of Fick's laws is given in [8].

As mentioned earlier, two types of diffusion most commonly occur in nature: self-diffusion and inter-diffusion. Self-diffusion involves diffusion of only one type of atom, while inter-diffusion covers diffusion of atoms of two or more different elemental types, e.g. Cu diffusing into Ni. The following section evaluates all the parameters and forces that influence the self-diffusion of atoms. This exercise yields important information on what happens to an atom during diffusion, e.g. what binding forces must be overcome, how the rate of diffusion is influenced by the natural vibration of all atoms, etc. If one understands self-diffusion, one can extend the analysis to inter-diffusion and perform diffusion calculations, even if the inter-diffusion coefficient is not available, by using the self-diffusion coefficient. This relation between the inter-diffusion coefficient and the self-diffusion coefficient will be addressed later on in this chapter.

2.3 Self-Diffusion

From the various studies performed on self-diffusion in metals it was discovered that the diffusion rate follows a simple Arrhenius relationship [9]

$$D = D_0 e^{-Q/kT}, \tag{2.4}$$

with D_0 the pre-exponential frequency factor, Q the activation energy, k Boltzmann's constant and T the absolute temperature. The pre-exponential factor and the activation energy can be found experimentally, but it is difficult to assign a physical meaning to these two parameters.

To clarify the diffusion equation and assist in estimating the diffusion coefficient, the various factors involved in diffusion (number of nearest neighbours, correlation factors, etc.) were incorporated into a random walk approach to diffusion. This led to an expression describing the pre-exponential factor in terms of entropy, lattice vibration frequency and other terms, while the activation energy was found to consist of enthalpy terms. The surface orientation dependence of the activation energy is also investigated in the following section.

2.3.1 Random Walk Diffusion

Equation (2.1) is normally derived from continuum diffusion equations [10], but it is sometimes more advantageous to describe diffusion in terms of actual atomic motion. To simulate the diffusion of atoms in a crystal lattice, a random walk process is applied to one atom in the crystal. This atom possesses a mean value of the properties associated with the entire system under investigation [10], so that the various components involved in diffusion is described by the random walk of the single atom. It is also assumed that for a particle performing a random walk in 2-dimensions (or 3-dimensions) the individual step distance is of equal length r [11].

Furthermore, all possible directions of motion have equal probability and successive atomic jumps are uncorrelated. A typical random walk process is shown in Figure 2.1.

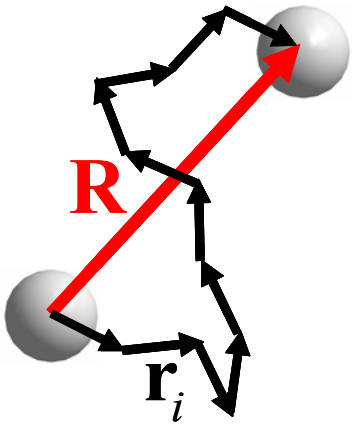

Figure 2.1: Illustration of a random walk performed by one particle. **R** is the distance the particle has moved from the origin and r_i represents the various jumps.

After a certain time, the atom undergoing a random walk process in a 2-dimensional crystal has performed *n* elementary jumps, and the distance the atom moved as a result of these elementary jumps is given by [10, 11]

$$\begin{aligned} R_n^2 &= nr^2 \\ &= t\Gamma r^2, \end{aligned} \tag{2.5}$$

where *t* represents time and Γ is the mean jump frequency of the atoms. If the random walk was performed in a 3-dimensional crystal, the distance the atom has moved, is given by

$$R_n^2 = n\overline{r^2} \tag{2.6}$$

which differs from equation (2.5) in that the elementary jump distance is now given by a root-mean-square jump distance [11]. The problem of relating the jump distance

to the diffusion coefficient was studied by Einstein, who found a now famous connection between the diffusion coefficient and jump distance [12] given by

$$6Dt = nr^2. \tag{2.7}$$

Solving equation (2.7) in terms of the diffusion coefficient and setting $\frac{n}{t} = \Gamma_0$ leads to

$$D = \tfrac{1}{6}\Gamma r^2. \tag{2.8}$$

As mentioned in the beginning of this section, it was assumed that successive jumps are uncorrelated for a random walk process. For real crystals, however, atomic jumps are correlated, and a correlation factor (*f*) is introduced to equation (2.8). In addition, the influence of the nearest neighbours on atomic motion must also be taken into account, and so the number of nearest neighbours (*z*) is also added to equation (2.8) which leads to

$$D = \tfrac{1}{6} zf\Gamma r^2 \tag{2.9}$$

If an atom is to move from one lattice position to another, it first encounters an energy barrier that it must overcome in order to execute the jump [11], an example of which is shown in Figure 2.2.

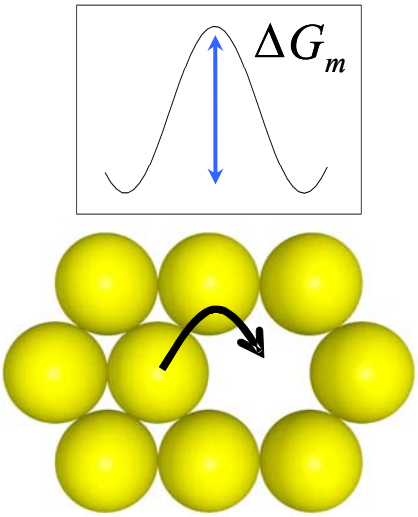

Figure 2.2: Representation of the energy barrier encountered by an atom while attempting a jump from one position to another.

The probability that it has enough energy to overcome this energy barrier at any one time is given by [11]

$$P_m = e^{\frac{-\Delta G_m}{kT}} \tag{2.10}$$

with k Boltzmann's constant, T the temperature and ΔG_m the change in the Gibbs free energy for migration, given by [13]

$$\Delta G_m = \Delta H_m - T\Delta S_m \tag{2.11}$$

with ΔH_m the enthalpy of migration and ΔS_m the entropy of migration.

If the atom does possess enough energy to overcome the energy barrier, it can only jump into a vacant lattice site [14] (see [8] for a discussion on the different types of

diffusion) and the probability that an adjacent lattice site is vacant is given by the mol fraction of vacancies that exist in a crystal [14]:

$$P_v = X_v = e^{\frac{-\Delta G_v}{kT}} \tag{2.12}$$

where

$$\Delta G_v = \Delta H_v - T\Delta S_v \tag{2.13}$$

and ΔH_v is the enthalpy of formation for one mol of vacancies and ΔS_v the excess entropy of one mol of vacancies.

The jump frequency term of equation (2.9) is a combination of the lattice vibration frequency, the probability of migration and the probability that an adjacent site is vacant, given by [14]

$$\Gamma = \Gamma_0 P_m P_v, \tag{2.14}$$

where the lattice vibration frequency Γ_0 is approximated by the Debye frequency of lattice vibration $\omega_D = \frac{k\theta_D}{h}$ [15,16,17].

Equation (2.14) is now inserted into equation (2.9), which leads to

$$D = \tfrac{1}{6} zfr^2 \left[e^{\left(-(\Delta H_m - T\Delta S_m)/kT\right)} \right] \left[e^{\left(-(\Delta H_v - T\Delta S_v)/kT\right)} \right] \Gamma_0. \quad (2.15)$$

The temperature dependent and independent terms are grouped together, resulting in:

$$D = \tfrac{1}{6} zfr^2 \Gamma_0 \left[e^{\left((\Delta S_m + \Delta S_v)/k\right)} \right] \left[e^{\left(-(\Delta H_m + \Delta H_v)/kT\right)} \right]. \quad (2.16)$$

Equation (2.16) is the same as equation (2.4), with

$$D_0 = \tfrac{1}{6} zfr^2 \Gamma_0 \left[e^{\left((\Delta S_m + \Delta S_v)/k\right)} \right] \quad (2.17)$$

and

$$Q = \Delta H_m + \Delta H_v, \quad (2.18)$$

sometimes also written as [13]

$$Q = E_m + E_V, \quad (2.19)$$

Methods of calculating the entropy terms in equation (2.17) are discussed in the following sections.

2.3.2 Estimating the entropy of migration

Dobson, et. al. [16] calculated the migration entropy of an atomic hop into a nearest-neighbour vacancy position. They assumed that the entropy is translational at the saddle-point configuration and vibrational at the initial equilibrium state before any hopping. The entropy contributions are calculated from statistical thermodynamics, where the translational entropy is found from a particle-in-a-box approximation and the vibrational entropy from that of a simple harmonic oscillator at the Debye frequency. This approach is different from the normally employed calculation in which the entropy of migration is calculated from [18, 19]

$$\frac{\Delta S_m}{k} = \sum_i \ln\left(\frac{\omega_i}{\omega_i'}\right)$$

where ω_i and ω_i' are the normal-mode frequencies at the initial and saddle-point configurations. The above method of calculation has two major drawbacks: (a) a potential is assumed for the above calculation, but the defect properties computed with the above method are quite sensitive to this potential and, furthermore, this potential is not known well enough to give accurate results; (b) one usually calculates force constants from this assumed potential and then employ the Einstein [18] approximation to calculate the various entropies. The Einstein approximation is, however, inaccurate enough so that one can question the validity of the numerical results [20].

To bypass these calculation problems, the present calculation of migration entropy proceeds from the ballistic-model (BM) hypothesis [16, 21, 22] which assumes that the atomic migration energy is kinetic in origin. In other words, a migrating atom must gain sufficient kinetic energy to overcome the saddle-point energy.

Therefore, in order to calculate the entropy of migration, the BM treatment is extended so that for temperatures above the Debye temperate, an atom on a normal lattice site can be modelled as a simple harmonic oscillator vibrating at the Debye frequency. The entropy associated with this vibration is calculated from [16, 17]

$$S_{vibrational} = 3k\left[\frac{h\omega_D/kT}{\exp\left(h\omega_D/kT\right)-1} - \ln\left[1-\exp\left(-h\omega_D/kT\right)\right]\right]. \qquad (2.20)$$

The factor 3 indicates three degrees of freedom.

Furthermore, the BM model states that when an atom moves through the saddle-point configuration, the hopping atom is nothing more than a free particle moving ballistically. The entropy of such a particle is given by [23]

$$S_{translational} = k\ln\left[\frac{\left(2\pi emkT\right)^{3/2}}{h^3}V\right] \qquad (2.21)$$

where $e = 2.718$, m is the mass of the migrating atom and V is the volume of the box occupied by two nearest neighbour atoms, taken as a tetrahedral [16]. The entropy

depends weakly on the volume V, such that any other reasonable way of approximating the volume is acceptable. The entropy of migration is then simply given by

$$\Delta S_m = S_{translational} - S_{vibrational}. \tag{2.22}$$

2.3.3 Estimating the vacancy formation entropy

As described in the previous section, entropy calculations proceeding from Einstein approximations and force constants yield entropies with dubious accuracy. For the migration entropy, a calculation method was used that does not depend on any of the aforementioned parameters. Similarly, the calculation of the vacancy formation energy is also done in a manner that excludes many problems described in the first paragraph of the previous section.

Burton, et. al. [20] calculated the entropy of vacancy formation for a number of FCC and BCC metals. They proposed a calculation in which the n atoms vibrate as coupled oscillators while the rest of the crystal is held fixed. The vibrational frequencies are

$$\omega_{n,n}(i) = \frac{1}{2\pi}\left(\frac{k_{n,n}(i)}{m}\right)^{1/2} \tag{2.23}$$

The entropy per atom is then given by

$$S_{n,n} = \frac{k}{n}\left[\frac{h\omega_{n,n}(i)/kT}{\exp\left(h\omega_{n,n}(i)/kT\right)-1} - \ln\left[1-\exp\left(-h\omega_{n,n}(i)/kT\right)\right]\right] \tag{2.24}$$

If a central atom is removed, the entropy of the $n-1$ atoms $\left(S_{n-1,n}\right)$ can be calculated as described above. The entropy of vacancy formation is then found from

$$\Delta S_n = (n-1)\left(S_{n-1,n} - S_{n,n}\right), \tag{2.25}$$

while the entropy of vacancy formation for an infinite lattice is given by

$$\Delta S_v = \lim_{n\to\infty} \Delta S^n . \tag{2.26}$$

A value of 1.89*k* for the present calculation for self-diffusion in copper compares well to the value of 1.5*k* obtained by Dobrzynski, et. al. [24] and a value of 1.67*k* obtained by Wynblatt, et. al. [19].

2.3.4 Estimating the Migration Energy

The migration energy is calculated with Flynn's model of vacancy migration [25]. In this model, Flynn showed that the jump frequency of atom-vacancy exchanges can be expressed as

$$\Gamma_v = \left(\tfrac{3}{5}\right)^{\frac{1}{2}} \omega_{\mathrm{D}}\, e^{-c\Omega\delta^2/kT} \tag{2.27}$$

where δ is a rough estimate of the critical displacement ratio from equilibrium needed to achieve vacancy-atom exchange, Ω is the atomic volume and c is an average elastic constant for migration given by

$$c = \frac{15\mu(\lambda + 2\mu)}{2(2\lambda + 7\mu)} \tag{2.28}$$

with λ and μ Lamé constants. Cubic crystals can also be considered to be anisotropic [25], so that equation (2.28) can be replaced by an average reciprocal modulus:

$$\frac{1}{c} = \frac{3}{c_{11}} + \frac{2}{c_{11} - c_{12}} + \frac{1}{c_{44}} \tag{2.29}$$

where c_{11}, c_{12} and c_{44} are elastic constants. The quantity $c\Omega\delta^2$ represents the migration energy barrier and is used to calculate the migration energy, listed in Table 2.1.

$\omega_D \ (\mathrm{s}^{-1})$	$\Delta S_m \ (k)$	$\Delta S_v \ (k)$	E_m (eV) [25]	$\mathrm{E_v^{111}}$ (eV)	$\mathrm{E_v^{100}}$ (eV)	$\mathrm{E_v^{110}}$ (eV)
6.67×10^{12}	6.58	1.89	0.84	1.54	1.34	1.07

Table 2.1: Summary of calculated values for the self-diffusion coefficient of copper. See text for discussion.

2.3.5 Vacancy formation Energy

Vacancy formation energy is defined as the difference between the energy required to remove an atom from the bulk and the energy gained when the atom is added onto the surface (ad-atom) [26], i.e.

$$E_v = E_{\text{Coh}}^{\text{Bulk}} - E_{\text{Coh}}^{\text{Surface}} \tag{2.30}$$

where E_{Coh}^{Bulk} is the cohesive binding energy for an atom in the bulk of a crystal and $E_{Coh}^{Surface}$ is the binding energy for an atom added onto the surface (ad-atom). These binding energies were calculated by Terblans, et. al. [27] using the empirical many-body Sutton-Chen potential

$$U = \varepsilon \sum_i \left[\tfrac{1}{2} \sum_{\substack{j=1 \\ j \neq i}} \left(\frac{a}{r_{ij}} \right)^n - c \left[\sum_{\substack{j=1 \\ j \neq i}} \left(\frac{a}{r_{ij}} \right)^n \right]^{1/2} \right] \tag{2.31}$$

with ε an energy parameter, c dimensionless parameter, a the lattice constant and r_{ij} is the distance between atoms i and j. Vacancy formation energies for different surface orientations are listed in Table **2.1**.

To evaluate the validity of the previous sections, a comparison was made between the calculated diffusion coefficient for the various surface orientations and the experimental diffusion coefficient of copper.

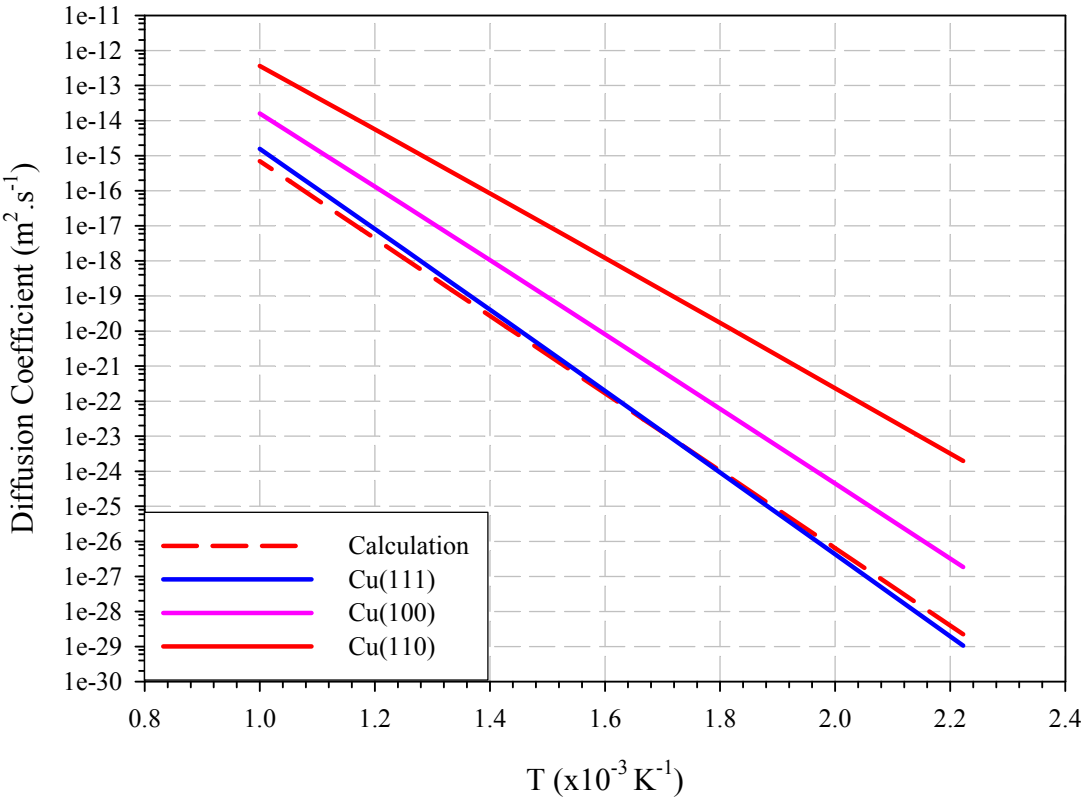

Figure 2.3: Comparison of the calculated and experimental self-diffusion coefficient of copper. Experimental data used for the different surface orientations taken from [27] and [28].

To achieve this, the constituent parts of equation (2.16) were calculated as described in the above text and an Arrhenius plot was constructed for the self-diffusion coefficient of copper with three different surface orientations, as shown in Figure 2.3. To aid in the evaluation of the calculated diffusion coefficient, experimental data [28] was also added to the Arrhenius graph. The calculated self-diffusion coefficient compares well with the experimental data, considering the large spread of the experimental data. The above calculation is applicable to a number of other FCC metals, e.g. Pt, Al, Pb, etc.

The next section covers inter-diffusion and different methods of solving Fick's second law that apply to inter-diffusion.

2.4 Inter-diffusion

Inter-diffusion is defined as the mutual diffusion of two or more different materials into one-another [29]. This process is also described by Fick's second law and can be solved either analytically or numerically, depending on the type of calculation involved. The analytical solution is a very fast solution, but it is limited to constant diffusion coefficients while the numerical solution is more involved but it allows varying diffusion coefficients and temperatures.

The importance of the diffusion coefficient becomes apparent when observing diffusion in binary and higher order alloys. In such a situation, D in equation (2.3) is an effective or coupled diffusion coefficient [30] composed of the intrinsic diffusion coefficients of the constituent parts A and B [29, 31], given by

$$D = D_A X_B + D_B X_A \tag{2.32}$$

with D_A and D_B the intrinsic diffusion coefficients of A and B respectively, while X_A and X_B is the fractional concentration of A and B. Equation (2.32) is also known as Darken's second equation [12, 31]. These intrinsic diffusion coefficients can be identified with the corresponding self-diffusion coefficients D_A^* and D_B^*, in which case equation (2.32) becomes

$$D = \left(D_A^* X_B + D_B^* X_A \right) \alpha_{AB} \tag{2.33}$$

where α_{AB} is a thermodynamic factor which represents the solution departure from ideality and is given by [30]

$$\alpha_{AB} = 1 + \frac{\partial \ln f_A}{\partial \ln X_A} = 1 + \frac{\partial \ln f_B}{\partial \ln X_B}. \tag{2.34}$$

where f_A and f_B is the activity coefficient of element *A* and *B* respectively. An in depth discussion of the activity coefficient is given in [8].

Equation (2.33) is sometimes referred to as the Darken-Hartley-Crank equation [12]. Both the numerical and analytical solution methods will now be discussed in the paragraphs below and the results of both calculations are compared to one another.

2.4.1 Analytical solution with a constant diffusion coefficient

Suppose a crystal has a thickness *L* and the surface of the crystal is located at $x = 0$. The diffusion source is also restricted to a layer with a thickness *h*. These boundary conditions can be expressed as follows [32]:

$$\begin{aligned} &0 \le x \le L; \\ &C(x) = 0 \text{ for } x > h \text{ and } t = 0; \\ &C(x) = C_0 \text{ for } 0 \le x \le h \text{ and } t = 0; \\ &\frac{\partial C}{\partial x} = 0 \text{ at } x = L \text{ for } t \ge 0. \end{aligned} \tag{2.35}$$

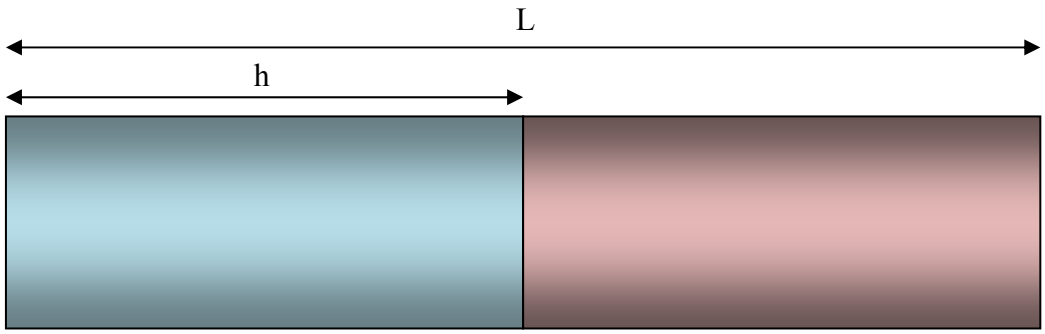

Figure 2.4: Graphical representation of the boundary conditions used to solve Fick's second law.

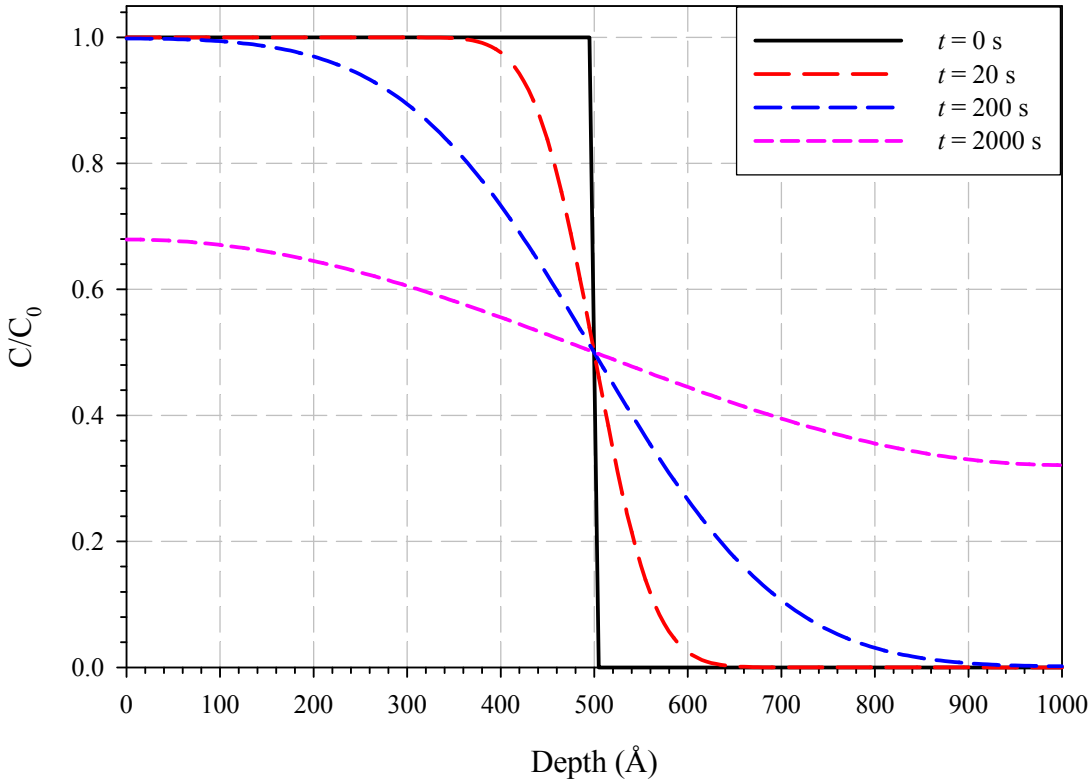

Figure 2.5: Analytical solution of Fick's second law for a finite sample with a limited diffusion source.

The parameters used for this calculation are: $D_0 = 1 \times 10^{-5}$ m^2.s^{-1}, $Q = 170$ kJ.mol^{-1}, $T = 400\ ^\circ C$.

The conditions listed in equation (2.35) are shown graphically in Figure 2.4. Using the boundary conditions described in equation (2.35), a solution for equation (2.3) is found to be [32]:

$$C = \frac{1}{2} C_0 \sum_{n=-\infty}^{\infty} \left(\operatorname{erf} \frac{h + 2nl - x}{2\sqrt{Dt}} + \operatorname{erf} \frac{h - 2nl + x}{2\sqrt{Dt}} \right). \tag{2.36}$$

An example solution of equation (2.36) is shown in Figure 2.5.

2.4.2 Numerical solution

The numerical solution of equation (2.3) is obtained by estimating the partial differential $\frac{\partial C}{\partial t}$ using a Taylor series in t as well as in x to obtain the difference quotient [33]

$$\frac{\partial C}{\partial t} = \frac{C_{t+k} - C_t}{k} + O\left(k^2\right) \tag{2.37}$$

and

$$\frac{\partial^2 C}{\partial x^2} = \frac{C^{x+h} - 2C^x + C^{x-h}}{h^2} + O\left(h^2\right) \tag{2.38}$$

with $C_{(t+k)}$ the concentration at time $t+k$, $C_{(t)}$ the concentration at time t, k the time integration step, $C^{(x+h)}$ the concentration at a distance $x+h$, $C^{(x)}$ the concentration at a distance x, $C^{(x-h)}$ the concentration at a distance $x-h$, h the spatial integration step, $O\left(k^2\right)$ and $O\left(h^2\right)$ the error. If the integration steps are sufficiently small, the errors are negligible and equation (2.3) can be written as

$$\frac{C_{t+k}^{j} - C_{t}^{j}}{k} = D\left(\frac{C^{j+1} - 2C^{j} + C^{j-1}}{h^2}\right) \tag{2.39}$$

with *j* the index of the current atomic layer.

Rearranging equation (2.39) yields an expression with which one can calculate the concentration in layer *j* [33]:

$$C_{t+k}^{j} = C_{t}^{j} + kD\left(\frac{C^{j+1} - 2C^{j} + C^{j-1}}{h^2}\right). \tag{2.40}$$

By repeating the calculation with equation (2.40) *n* times, a concentration profile is calculated after a time $t = nk$.

As previously mentioned, a numerical solution of equation (2.3) allows a variable (discussed in chapter 4) diffusion coefficient to be introduced, but the calculation time is significantly longer than the analytical solution discussed in the previous paragraph. As verification of the validity of equation (2.40), a comparison was made between the numerical and analytical solutions of Fick's second law in Figure 2.6 for $D_0 = 1\times10^{-5}$ $\mathrm{m^2.s^{-1}}$, $Q = 170$ $\mathrm{kJ.mol^{-1}}$ and $T = 400$ °C.

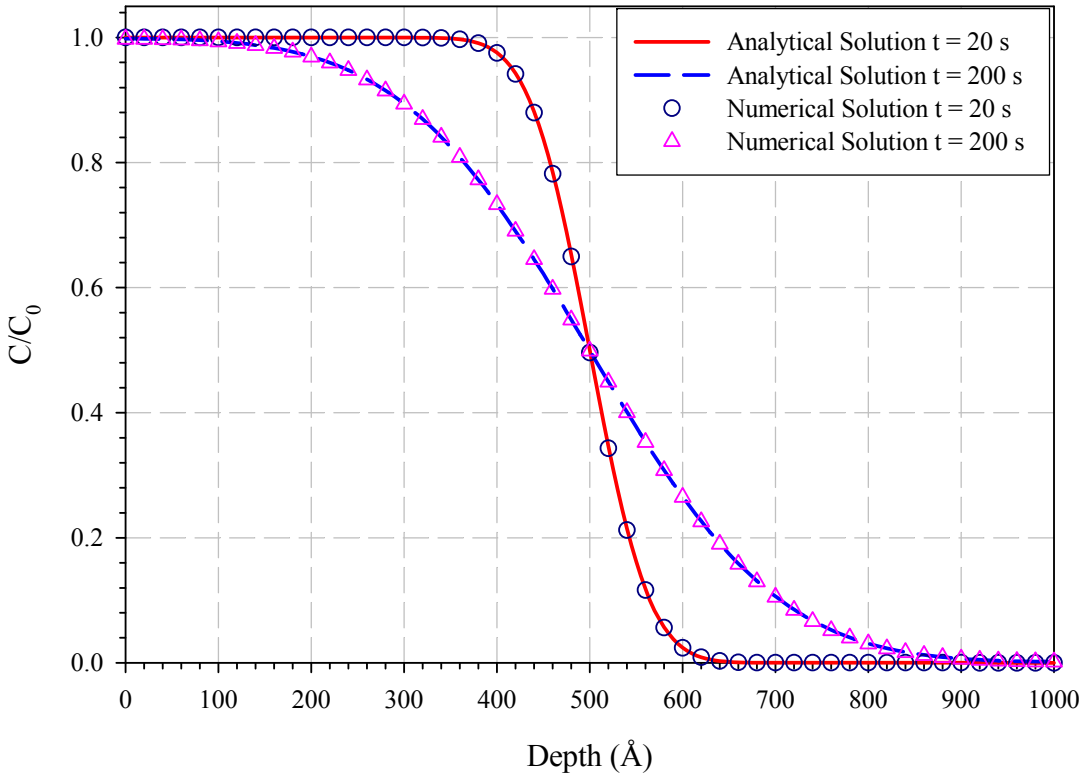

Figure 2.6: Comparison of numerical and analytical solution of Fick's second law. The parameters used for this calculation are the same as Figure 2.5. The numerical solution closely follows the analytical solution.

In the situation discussed above, the analytical solution is the easier of the two types of methods to solve. For a different type of situation, e.g. a periodic multilayer system, the analytical solution becomes a mathematically complex method, while the numerical solution can be applied to a periodic multilayer with virtually no adjustment to the calculation routine. For the purposes of this study, the numerical solution proved invaluable since temperature ramping was easily incorporated into the calculation routine. This incorporation is discussed in chapter 4.

Now that diffusion has been discussed in some detail, the theories discussed above can be applied to experimental diffusion studies. However, there is a significant

difference between calculated inter-diffusion profiles and measured inter-diffusion profiles, as the experimental profile is altered by the analysis technique used to study a sample. The next chapter introduces the concept of a depth resolution function which describes the altering of a sample due to the analysis technique, and also provides methods for profile reconstruction to assist in the analysis of experimental data.

Chapter 3 – Depth Profile Reconstruction

3.1 Introduction

While the previous chapter dealt with theoretical aspects of self-diffusion and inter-diffusion, experimental studies of diffusion are as important, if not more so, than the theoretical studies. Quite often, an experimentalist would be interested in the chemical composition of a sample below the surface, also called depth profiling [34]. This analysis technique enables engineers and scientists to study microelectronic devices, corrosion resistant surfaces and characterizing plasma modified surfaces, among others [34].

Several different techniques exist for obtaining said depth profile, e.g. ion scattering spectroscopy (ISS), secondary-ion mass spectroscopy (SIMS), x-ray photoelectrons spectroscopy (XPS), glow discharge spectroscopy, and last but not least, Auger electron spectroscopy (AES) [35]. In all of the techniques mentioned, ion erosion is often employed to etch away the sample while simultaneously monitoring the exposed surface to obtain a composition versus depth profile.

However, during erosion, the composition of the exposed surface layer, and several atomic layers beneath the exposed surface, changes as a result of the impinging ions on the surface. This interaction modifies the composition of the sample and results in an altered depth profile when compared to the original profile. This complicates the analysis of the measured profile, as one needs to compensate for the changes in the

profile due to ion beam interactions with the sample [35]. Other effects that also need to be compensated for are the information depth from which the analysis technique obtains the chemical composition of the surface and also the roughening of the surface due to ion erosion. All of these effects influence the measured profile and contribute to what is known as the depth resolution function (DRF). If the DRF is well defined, one can obtain the original in-depth composition from the measured data [35]. This process is what is known as depth profile reconstruction.

This chapter deals with depth profile reconstruction in some detail, discussing the concept of the DRF and the Mixing-Roughness-Information model developed by Hofmann, et. al [36] to reconstruct depth profiles.

3.2 Depth Resolution

Studies focusing on optimizing the depth resolution (DR) of apparatus started in the mid 1970's [36]. According to the IUPAC and the ASTM E-42 committee, the depth resolution is the "depth range over which a signal increases or decreases by a specified amount when profiling through an ideally sharp interface between two media" [37]. By convention, the depth resolution is the distance over which an 84 % to 16 % change in signal is measured, shown in Figure 3.1. If the resulting profile can be approximated with an error function, the depth resolution (Δz) is described by the standard deviation of the corresponding Gaussian resolution function [37].

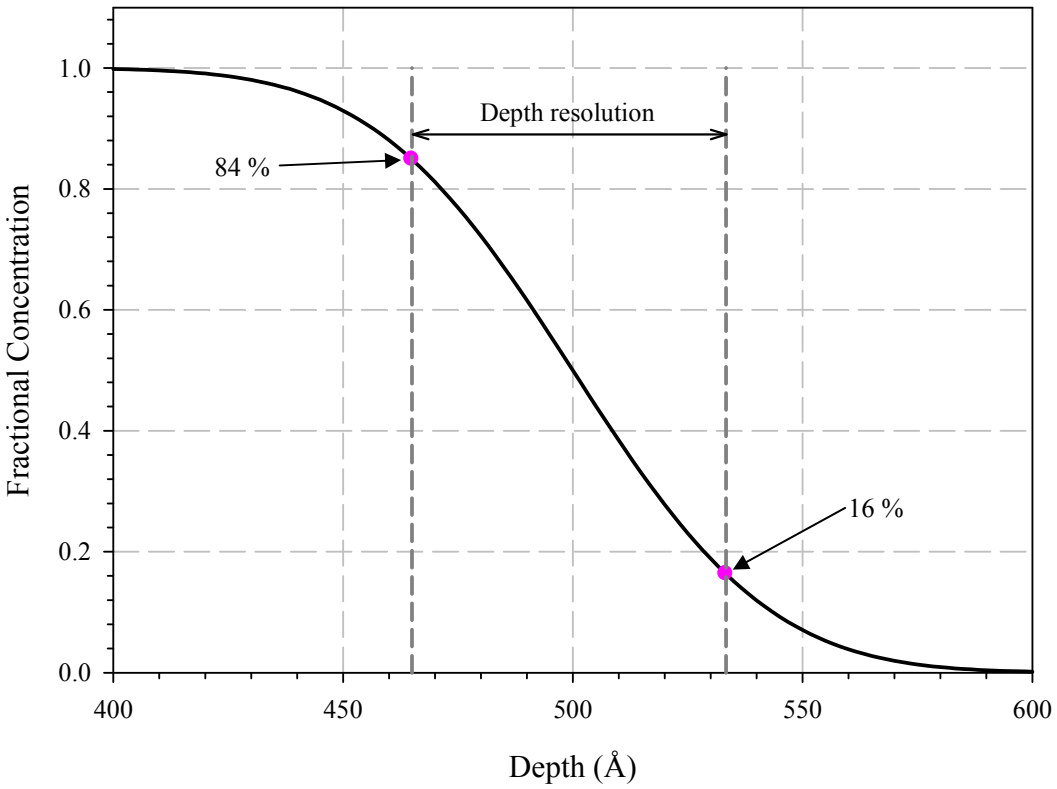

Figure 3.1: Graphical representation of the depth resolution.

For AES, the depth resolution is usually written as a combination of the intrinsic roughness of the sample due to preparation (Δz_0), surface roughening by sputtering statistics (Δz_s), atomic mixing and preferential sputtering (Δz_m), escape depth of the Auger electrons (Δz_λ) (also called the information depth) and the ion induced sputtering roughness (Δz_r) [38]. Experimental and theoretical studies showed that all the aforementioned components add up in quadrature to the DR [37, 38]

$$\Delta z = \left(\Delta z_0^2 + \Delta z_s^2 + \Delta z_m^2 + \Delta z_\lambda^2 + \Delta z_r^2 + \ldots\right)^{1/2}. \qquad (3.1)$$

Even though the DR is a simple enough concept, evaluation of data that are convoluted by the DR requires a more in-depth knowledge of the factors discussed above. These mechanisms contribute to a function that is responsible for the deviation of the measured profile. This function is known as the depth resolution function and is discussed in the next section.

3.3 Depth resolution Function

Sputter depth profiling can be viewed as a process that transforms an original compositional distribution into a distorted, measured profile, described by a convolution integral [35]

$$\frac{I(z)}{I_0} = \int_{-\infty}^{\infty} X(z')g(z-z')dz' \tag{3.2}$$

where $\frac{I(z)}{I_0}$ is the normalized, measured intensity at a sputtered depth z, $X(z')$ is the fractional concentration of the element being monitored at the original depth z' and $g(z-z')$ is the DRF. Equation (3.2) is usually solved by a forward calculation, which starts from the premise of assuming the value of $X(z')$, calculating the compositional profile and then comparing it to the measured profile. This process is repeated until the best fit between the calculated and measured profiles is obtained [37].

The DRF can also be solved by a more direct reverse calculation employing inverse Fourier transformation schemes, but this method suffers from experimental data that is not accurate enough and a very high signal-to-noise ratio [37]. The forward calculation method is favoured over the reverse calculation method for its simplicity and is the currently the most frequently used method.

Over the past 30-40 years, the factors that influence the depth resolution have received a lot of attention and several theoretical models were developed to determine the DR and the depth resolution function (DRF). Initially, Gaussian DRFs were used as the interfaces followed an error-function type broadening [35]. Any asymmetry in the measure profile was attributed to a knock-on effect as a result of the sputtering [37]. High incident angle ion beams and sample rotation resulted in depth profiles that were predominantly influenced by atomic mixing and less influenced by the surface roughness [37]. This implies that the depth resolution of the measurement apparatus increased substantially. However, these improvements led to an asymmetrical DRF (as a result of atomic mixing). Theoretical calculations followed rapidly and the first type of models to simulate the broadening of the interface was diffusional type models [37]. With the increase in calculation power of computers, Monte Carlo calculations appeared, while more recently research groups [39] employed SRIM (stopping range of ions in materials) type calculations combined with molecular dynamics calculations so simulate atomic mixing. While these calculations describe atomic mixing very well, they require a host of parameters which have an unpredictable influence on the calculations.

Semi-empirical and empirical models also describe the DRF with a high level of accuracy [35] and are considerably less complicated. The recently developed Mixing Roughness Information model (MRI) [36] employs a semi-empirical DRF that is based on three fundamental profiling parameters: atomic mixing, surface roughness and information depth. Using these parameters, the MRI model gives a mathematical description of the DRF which is easy to implement. During this study, the MRI model was used to assist in the analysis of experimental data and therefore deserves a detailed discussion, presented below.

3.4 Description of the MRI model

At its heart, the MRI model uses three mathematical equations to describe the DRF:

$$\text{Atomic Mixing: } g(z) = \exp\left(\frac{-(z - z_0 + w)}{w}\right) \tag{3.3}$$

$$\text{Information Depth: } g(z) = \exp\left(\frac{-(z - z_0)}{\lambda}\right) \tag{3.4}$$

$$\text{Surface Roughness: } g(z) = \frac{1}{\sigma\sqrt{2\pi}} \exp\left(\frac{-(z - z_0)^2}{2\sigma^2}\right) \tag{3.5}$$

where z_0 denotes the position of the delta layer (position of the interface), z the current position in the sample, w the atomic mixing length, λ the information depth and σ the surface roughness. The three functions listed above are applied sequentially the contribution of each the functions is summed. The result is a calculated depth profile that one can compare to the measured depth profile.

The advantage of using the MRI model in depth profile analysis is that it is based on physical parameters that can easily be determined from measurements of reference materials [40]. The disadvantage is that it ignores several effects that have a marked influence on the depth profile, e.g. the non-linear relation between sputter time and depth. Even with these disadvantages, the MRI model is still a powerful tool in analysing measured depth profiles.

The implementation of the MRI model is discussed in the following sections.

3.4.1 Atomic Mixing

Sputter profiling with ions that impinge on a target surface result in a change of composition in first few atomic layers. The impinging ions interact with the target atoms and collisions and energy transfer takes place. The energy transferred to the target atoms from the incoming ions must be greater than the binding energy of the surface for target atoms to be removed. The number of atoms removed is very small and most of the energy transferred to the target results in cascade mixing.

As mentioned in the previous section, there exists a number of complex mathematical descriptions for sputter induced atomic mixing. The MRI model, on the other hand, approaches atomic mixing in a slightly simpler fashion by assuming instantaneous mixing and the formation of a homogeneous area with a width *w*. This area is created after a certain sputtered depth [36] and remains constant with sputtered depth. Furthermore, the sputtering rate is also assumed constant for the different elements in the sample.

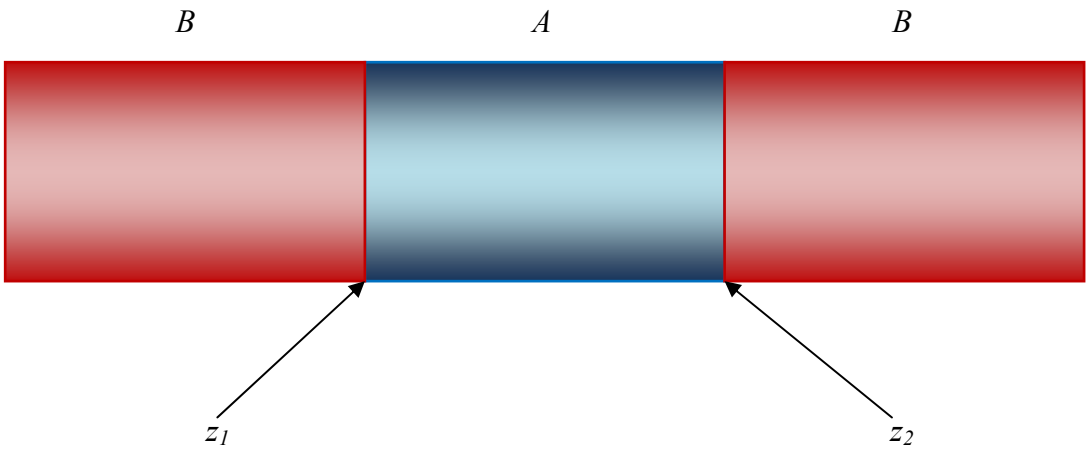

Figure 3.2: Representation of the multilayer setup used in the MRI model. *A* and *B* represent thin layers of the two materials under investigation and $z_1$and z_2 are the interface positions.

If one now considers a two component system, *A* and *B*, the concentration of A $\left(X_A\right)$ in a matrix *B* at a sputtered depth of *z* is given by [36]

$$\frac{dX_A}{dz} = \frac{1}{w}\left(X^0_{A(z+w)} - X_A\right) \tag{3.6}$$

with $X^0_{A(z+w)}$ the original concentration of *A* at a distance *w* in front of the instantaneous surface *z*.

If one applies the MRI model, i.e. solve equation (3.6), for a multilayer *B*/*A*/*B* structure with abrupt interfaces z_1 and z_2 shown in Figure 3.2, equation (3.6) has a solution of the form [36]

$$X^l_A = X^0_A\left(1 - e^{-\frac{z-z_1-w}{w}}\right) \tag{3.7}$$

for the leading edge (*B*/*A*) and

$$X_A^t = X_A^0 e^{-\frac{z-z_2-w}{w}} \tag{3.8}$$

for the trailing edge (*A*/*B*). Equation (3.7) holds when $z_1 - w \le z \le z_2 - w$ and equation (3.8) is valid when $z \ge z_2 - w$.

3.4.2 Surface roughness

During ion sputtering, the ion beam roughens the surface. The effect is minimized by rastering the beam and/or rotating the sample. Polycrystalline samples are particularly susceptible to degradation of the depth resolution as a result of surface roughening [41]. According to Wöhner, et. al. [41], the surface roughening is a direct result of the variation of the local sputtering rate of every grain microplane. The local sputtering rate in turn depends on the ion incidence angle and the crystallographic structure. Ref. [41] attempted to evaluate the influence of sputter-induced surface roughening by dividing the sample into a large number of vertical columns according to the crystallites with a variable grain size. The MRI model uses a simpler, yet effective, approach by describing the surface roughening as a superposition of a normalized Gaussian function broadening, given by [36]

$$X_A^b = \frac{1}{\sqrt{2\pi\sigma}} \int_{z-3\sigma}^{z+3\sigma} X_A^{l,t}(z') \cdot e^{\frac{-(z-z')^2}{2\sigma^2}} dz' \tag{3.9}$$

To ease numerical calculations, the limits of the integral are reduced from infinity to $z+3\sigma$ and $z-3\sigma$.

3.4.3 Information Depth

In AES and XPS, the information recorded by the apparatus is not limited to the first atomic layer only but is defined as a depth of approximately 3-5 times the escape depth of Auger electrons. The MRI model uses a simpler definition where the escape depth is the information depth and this effect is incorporated into the MRI model by using the equation [36]

$$\left(\frac{I_A}{I_A^0}\right)_t = X_A^t\left(1-e^{-\frac{w}{\lambda}}\right) \tag{3.10}$$

for the trailing edge and

$$\left(\frac{I_A}{I_A^0}\right)_l = X_A^l\left[1-e^{-\frac{w}{\lambda}}\right]+e^{-\frac{w}{\lambda}}\cdot\left[1-e^{-\frac{z_2-z-w}{\lambda}}\right] \tag{3.11}$$

for the leading edge. Equation (3.11) is only valid when $z+w\le z_2$.

Equations (3.7) to (3.11) constitute the MRI model. The MRI model can reconstruct depth profiles accurately, but this is not the only use of the model. Another use of the MRI model is in the determination of the inter-diffusion coefficient from depth profiles in which diffusion has taken place.

3.5 The MRI model and the diffusion coefficient

The solution of Fick's second law, equation (2.3), can be obtained for a variety of initial and boundary conditions, if the diffusion coefficient is constant [32]. Two examples of such solutions were given in the previous chapter. It is also possible to prove that by differentiating the following equation, a solution of Fick's second law is obtained [32]:

$$C = \frac{M}{2(\pi Dt)^{1/2}} \exp\left(-\frac{z^2}{4Dt}\right) \tag{3.12}$$

with M the amount of transported material. For a complete derivation of equation (3.12), the reader is referred to Crank, et. al. [32].

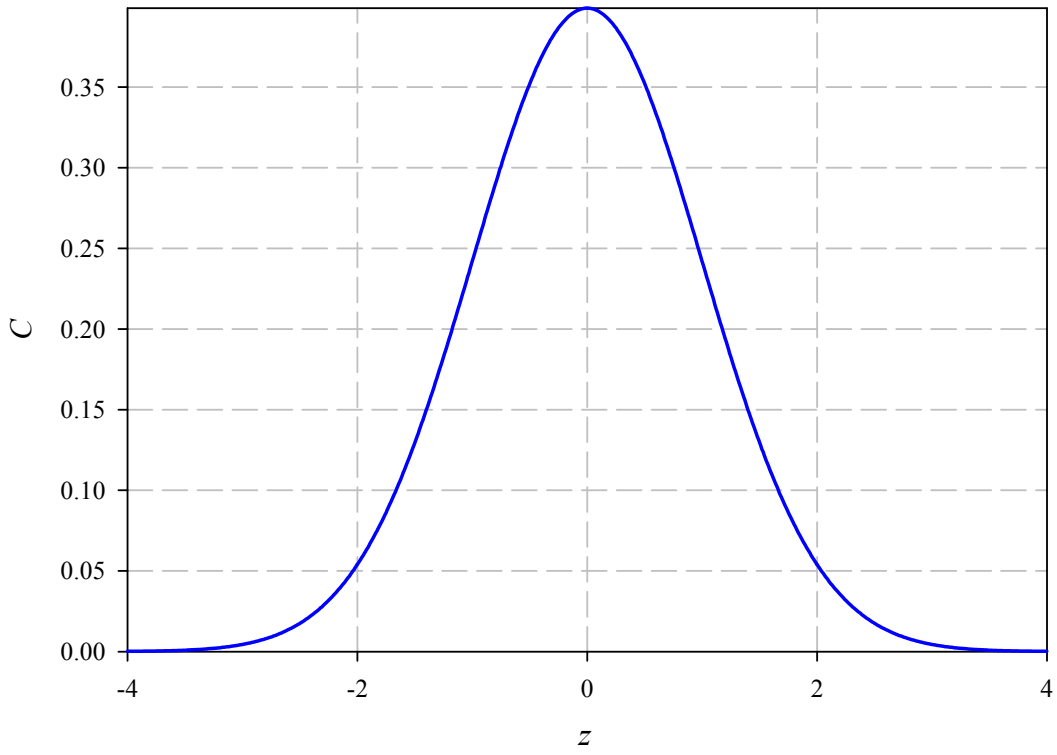

Figure 3.3: Example of a concentration-distance curves for an instantaneous plane source.

Equation (3.12) is a standard Gaussian function which represents the broadening of a profile with respect to time for a particular diffusion coefficient *D*, shown in Figure 3.3. This particular solution is applicable to an instantaneous plane diffusion source.

The MRI model describes the interface broadening or roughness as a Gaussian function, given by $\sim \exp\left(\frac{-(\Delta z)^2}{2\sigma^2}\right)$, with Δz representing depth. If one now assumes that the diffusion-induced depth profile can be written as a Gaussian function of the original concentration profile given by $\sim \exp\left(\frac{-(\Delta z)^2}{4Dt}\right)$ [38] (see equation (3.12)), the diffusion length is described by $\sqrt{2Dt}$. The diffusion length can then be equated to the broadening of the interface roughness by [38]

$$2Dt = \Delta\sigma^2 = \sigma_T^2 - \sigma_0^2 \tag{3.13}$$

with *t* the annealing time, σ_T the surface roughness parameter at a temperature *T* and σ_0 the surface roughness parameter of the reference sample.

According to ref. [38], the atomic mixing and information depth is depth independent while the surface roughness linearly increases with depth. If a reference sample is used to determine the independent parameters of the MRI model, then the MRI model can be used to calculate depth profiles for annealed samples by only changing the surface roughness parameter.

Then, from the change in the surface roughness parameter, the diffusion coefficient can be calculated, and if enough samples are analyzed, the pre-exponential factor D_0 and the activation energy Q can be calculated. This approach was employed in this study to determine the inter-diffusion coefficient of nickel in copper by means of a classical annealing method as well as a linear heating method. Both these experimental techniques are discussed in a later chapter.

The following chapter focuses on the effect that the annealing method has on the measured diffusion profile and proposes a new method for eliminating uncertainties associated with the annealing process.

Chapter 4 – Influence of heating on fast diffusing species

4.1 Introduction

The two previous chapters discussed the diffusion coefficient and methods of reconstructing measured depth profiles. This chapter deals with the effect the heating method has on the measured diffusion profile, and hence the diffusion coefficients obtained from such profiles.

Normally, thin film samples (of the order of thousands of Angströms) are annealed at different temperatures and different times, with the time of annealing taken as the difference between the time of insertion and removal from the furnace (see e.g. ref [42]). However, the sample's temperature does not increase nor cool down instantly when it is inserted and removed from the furnace. Instead, the sample temperature increases and decreases at a rate that depends on the surrounding environment and the sample itself. If the sample finds itself in a gas atmosphere when inserted into the furnace, the sample will heat up as a result of radiation as well as convection, and will similarly cool down as a result of radiation and convection (depending on the setup, heat conduction may also take place) [43]. These principles are well documented in most undergraduate physics manuals. To prevent chemical interaction between the sample and the surrounding atmosphere, annealing is often performed in a vacuum, where heat is transferred only by radiation.

To determine what effect the heat transfer mechanism has on annealing, one must incorporate the heat transfer mechanism into diffusion calculations. For the present study, the process of analysing the effect of annealing on diffusion can be summarized in three steps: 1) perform a diffusion calculation using the time between insertion and removal of a sample from a furnace (classical heating), 2) incorporating heating and cooling via radiation into the calculation (actual heating) and 3) the proposed development of a linear temperature ramp that allows one to control the heating and cooling involved in the diffusion process (linear heating).

The diffusion calculation used to study the influence of annealing environments involves the solution of Fick's second law for a constant and variable diffusion coefficient. The variable diffusion coefficient is needed when calculating the diffusion penetration curves while the temperature is changed during a calculation, which allows the diffusion rate to vary along with the varying temperatures. The incorporation of heating and cooling into the solution of Fick's second law is discussed below.

4.2 Incorporating radiative heating/cooling into the diffusion coefficient

The cooling of a body in a vacuum is mainly as a result of the energy loss due to thermal radiation.

The rate at which an object in a vacuum absorbs or emits radiation is given by the Stefan-Boltzman relation [43]

$$\Delta P_{rad} = \sigma e A\left(T_0^4 - T^4\right) \tag{4.1}$$

where σ is the Stefan-Boltzman constant, A is the area, e is the emissivity, T the temperature of the sample and T_0 the temperature of the environment. The emissivity e is a characteristic property of the material being studied and can be found in literature, however, since the emissivity is highly dependent on the type and surface properties of the material, varying values for the emissivity is often found in literature [e.g. 44, 45].

To circumvent this problem, the emissivity was determined from an experimentally measured heating and cooling profile for a specific experimental setup. The measured profile was obtained in atmosphere using a stainless steel sample (dimensions $10.6\ \text{mm} \times 10.6\ \text{mm} \times 0.8\ \text{mm}$) heated in a Lindburg furnace and the resulting profile is shown in Figure 4.1. A stainless steel sample was chosen as it is easier to spot weld the thermocouple onto the sample.

In order to calculate the theoretical heating/cooling profile, equation (4.1) was modified to include the transfer of heat due to convection [45]:

$$P = hA\left(T_0 - T\right) + \sigma e A\left(T_0^4 - T^4\right) \tag{4.2}$$

with h the heat transfer coefficient.

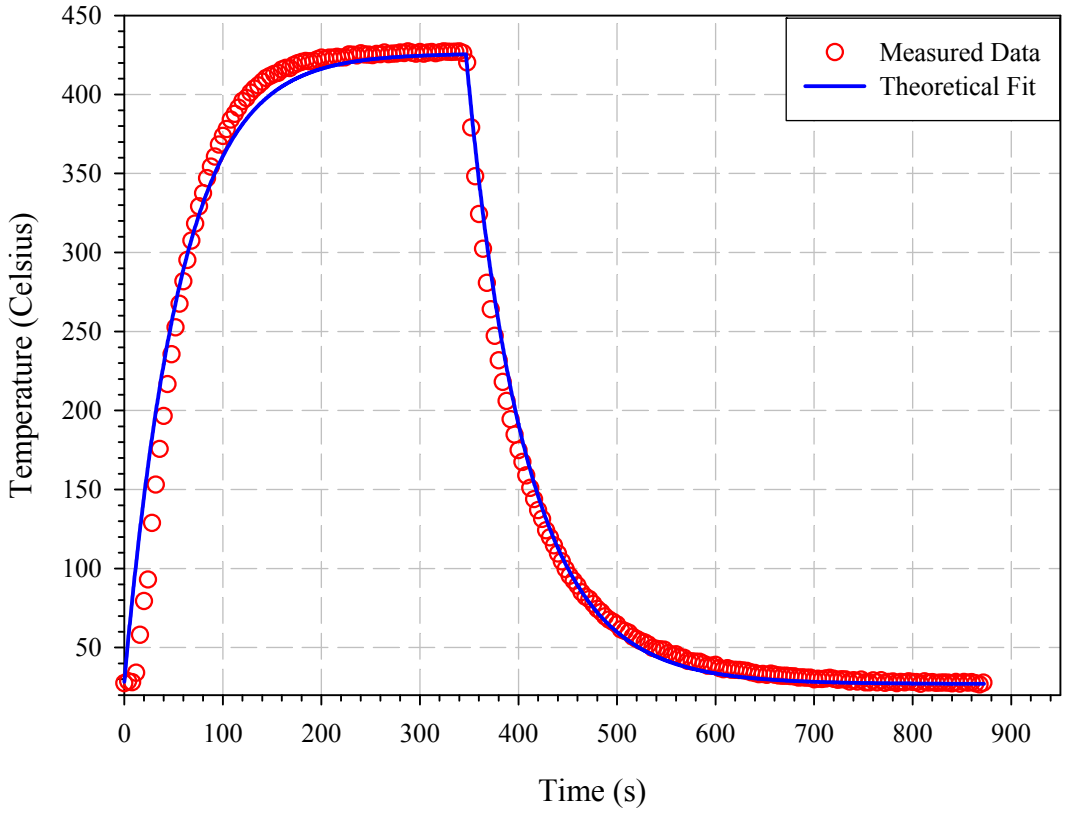

Figure 4.1: Experimentally measured and calculated heating and cooling profile for a stainless steel sample in atmosphere. See text for details.

The rate of heat transfer (eqs. (4.1) and (4.2)) can be related to the amount of energy Q gained or lost by [43]:

$$\Delta P = Q/\Delta t \tag{4.3}$$

with Δt a small time step in which the energy is lost/gained, and from equation (4.3), the temperature of the sample after a small time Δt can be calculated with [43]

$$Q = mc\left(T_f - T_i\right) \tag{4.4}$$

where T_f is the final temperature of the sample, T_i is the initial temperature of the sample, c is the specific heat of stainless steel with a value of $c = 500\ \text{J.}\left(\text{kg.K}\right)^{-1}$ [44] and m is the mass of the sample, with a measured value of $m = 666.95\ \text{mg}$. The algorithm that was used to incorporate the slow/linear heating and cooling into the numerical solution of Fick's second law is shown in the flow chart in Figure 4.2.

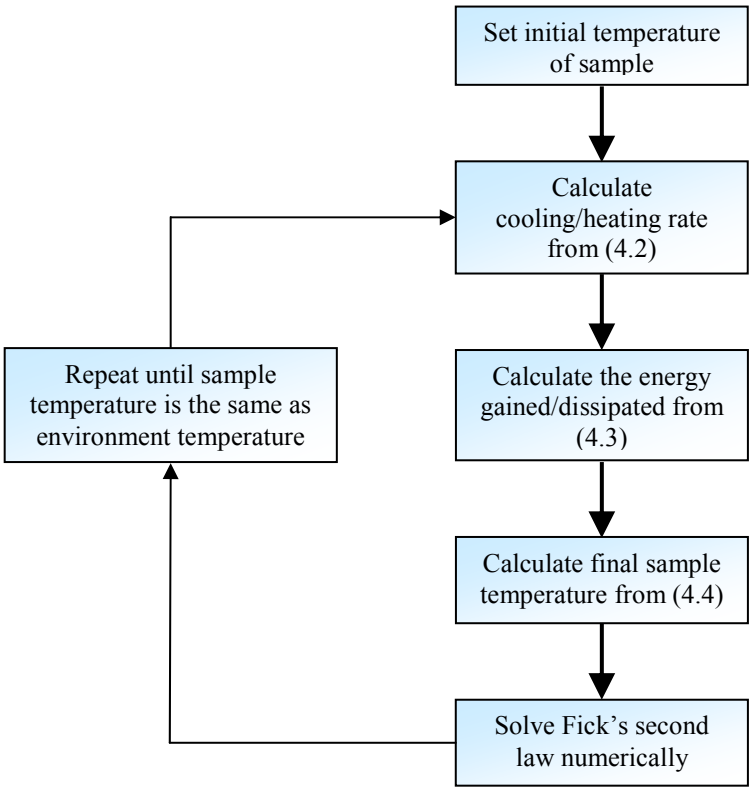

Figure 4.2: Calculation procedure used for incorporating heating and cooling into the numerical solution of Fick's second law.

To obtain a theoretical fit of the experimental data shown in Figure 4.1, the emissivity of the stainless steel sample and the heat transfer coefficient of air are needed.

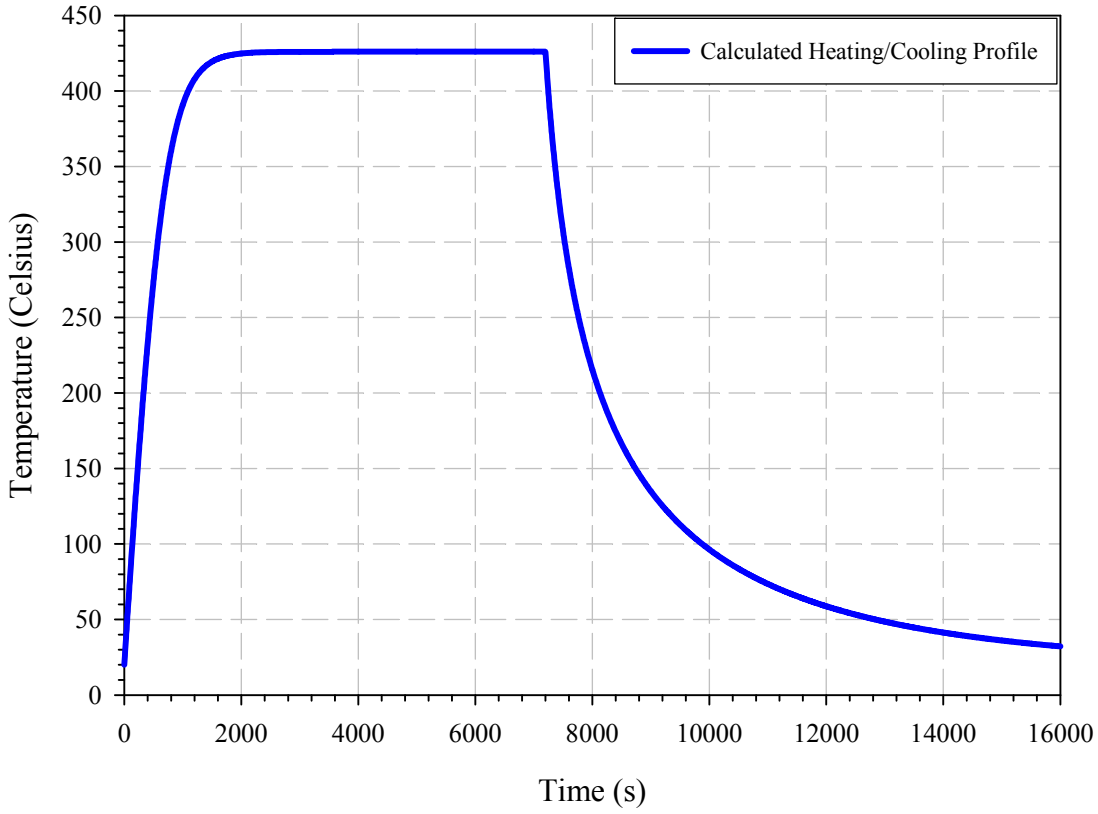

Figure 4.3: Heating/cooling profile calculated for the stainless steel sample discussed in the text, annealed for 7200 s.

A Nelder-Mead minimization routine [46] was implemented in order to find the emissivity and the heat transfer coefficient, which returned values of $e = 0.058$ and $h = 20.27\ \mathrm{W.(m^2.K)^{-1}}$.

The value obtained for h falls within the realistic value of $h < 25$ as stated in ref. [45], and the theoretical fit closely follows the experimental data in Figure 4.1. A heating and cooling profile in vacuum was also calculated for the stainless steel sample and is shown in Figure 4.3 from which it can be seen that convection speeds up heating and cooling considerably.

D_0 $\left(\mathrm{m^2.s^{-1}}\right)$	Q $\left(\mathrm{kJ.mol^{-1}}\right)$	**Temperature (Celsius)**	**Crystal Width (Å)**	**h (Å)**	**k (s)**	**Calculation Times (minutes)**
1×10^{-5}	170	400	2000	2	0.01	4, 120

Table 4.1: Parameters used in the inter-diffusion calculation.

The method to calculate the heating and cooling profile can be easily incorporated into a numerical solution of Fick's second law and such incorporation allows one to simulate the effect of actual heating on diffusion. To illustrate the effect of actual heating, several diffusion calculations were performed with the parameters listed in Table 4.1.

For the sample annealed for 4 minutes, the diffusion penetration curve is shown in Figure 4.4. There is no visible diffusion that took place at this temperature and annealing time for the actual annealing regime. As the annealing time is increased, the diffusion profile obtained using the actual heating process starts to approach the classical heating process, as shown in Figure 4.5. These results indicate that diffusion profiles of fast-diffusing species, annealed at low temperatures and for short times, will differ from the diffusion profiles obtained from the classical heating regime.

However, for long annealing times, the diffusion profiles of actual and classical heating approach one-another, i.e. classical heating analysis methods can be applied to studies that focus on slow-diffusing species, annealed for long periods of time.

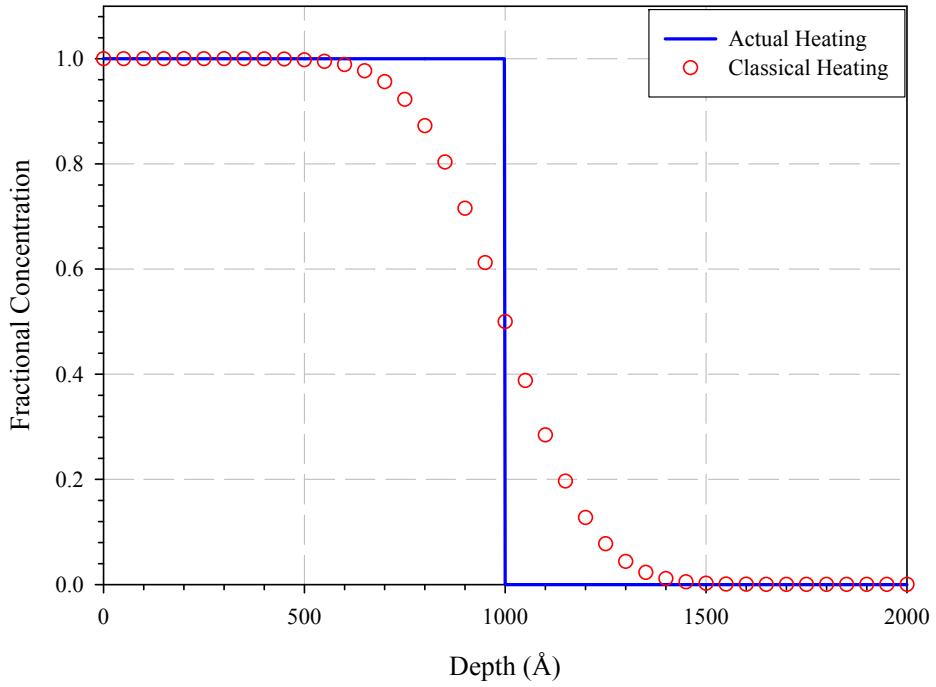

Figure 4.4: Diffusion penetration curve for a sample annealed for 4 minutes.

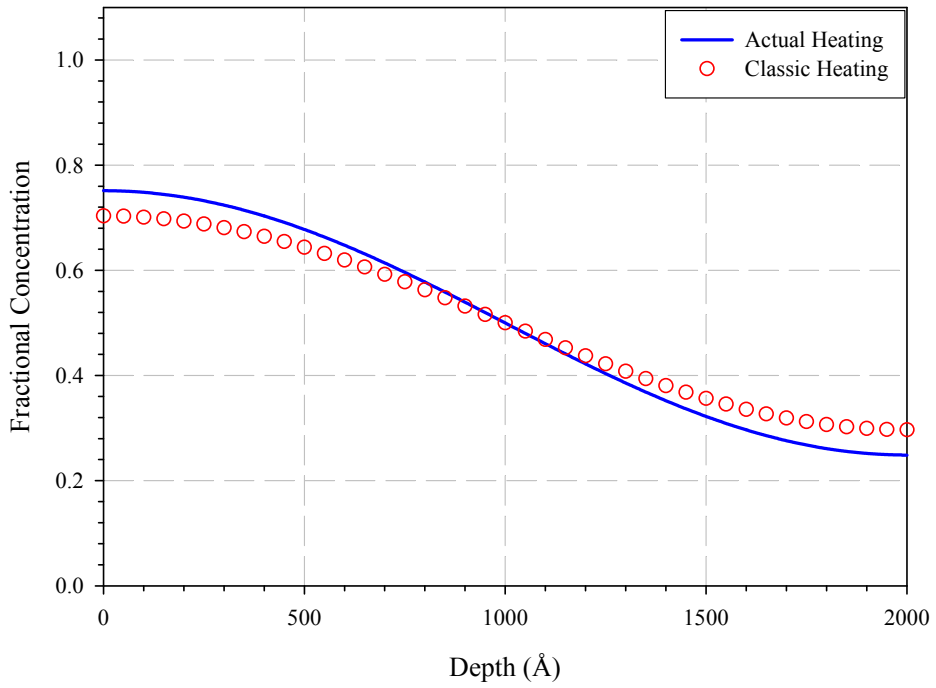

Figure 4.5: Diffusion penetration curve for a sample annealed for 120 minutes.

A criticism that can be levelled at the approach described above is the extraction of the emissivity from heating/cooling profiles measured in atmosphere. Even though the calculated conductivity of air falls within realistic values, it does not guarantee the correctness of the emissivity

The question of the emissivity can be bypassed completely if one controls the heating and cooling rate of the sample. A way of ensuring such control is to mount the sample into a programmable heating unit that can linearly ramp the temperature up and down in a vacuum. If one then incorporates linear heating into the numerical solution of Fick's second law in conjunction with the Nelder-Mead minimization technique, one can extract inter-diffusion parameters from experimentally ramped diffusion profiles. The drawback of this solution method is that it is extremely time-intensive, requiring full numerical solutions for each step in the Nelder-Mead process.

Using a full numerical solution in conjunction with the recursive Nelder-Mead technique is not practical, and an alternate method of analysing diffusion profiles obtained from linear ramp annealing is proposed below.

4.3 MRI Linear Ramping Approach

As mentioned previously, most diffusion studies rely on a constant, well defined annealing time which ignores heat transfer mechanisms and the MRI model is no different in this respect. If the temperature of a sample can be controlled with a linear heating scheme, the uncertainty of heat transfer is eliminated and the diffusion parameters obtained will also be more accurate. Unfortunately, the MRI model does

not cater for linear ramping. The only way to incorporate linear ramping in the MRI model is to equate the linear ramping heat treatment to a classical heat treatment. This classical heat treatment is an ideal heat treatment, or a perfect classical heat treatment, i.e. the sample temperature increases and decreases instantaneously. Heat transfer mechanisms are ignored as well.

The difficulty in reconciling linear ramping to classical annealing arises from the varying diffusion coefficient that is found when ramping the temperature of a sample. An example of the varying diffusion coefficient is shown in Figure 4.6, which was constructed by calculating the diffusion coefficient at each point during the temperature ramp from the diffusion parameters obtained from a classical annealing analysis. For a perfect classical anneal, the temperature stays constant throughout the annealing time and the diffusion coefficient also remains constant, an example of which is also shown in Figure 4.6.

One way to equate the two different methods of annealing is to assume that if the amount of energy transferred to a sample during a classical anneal is the same as the amount of energy transferred during a linear ramp anneal, the diffusion profiles obtained for the different annealing methods should also be the same.

The energy transferred to the ramped sample can be represented by the area underneath the curve shown in Figure 4.6.

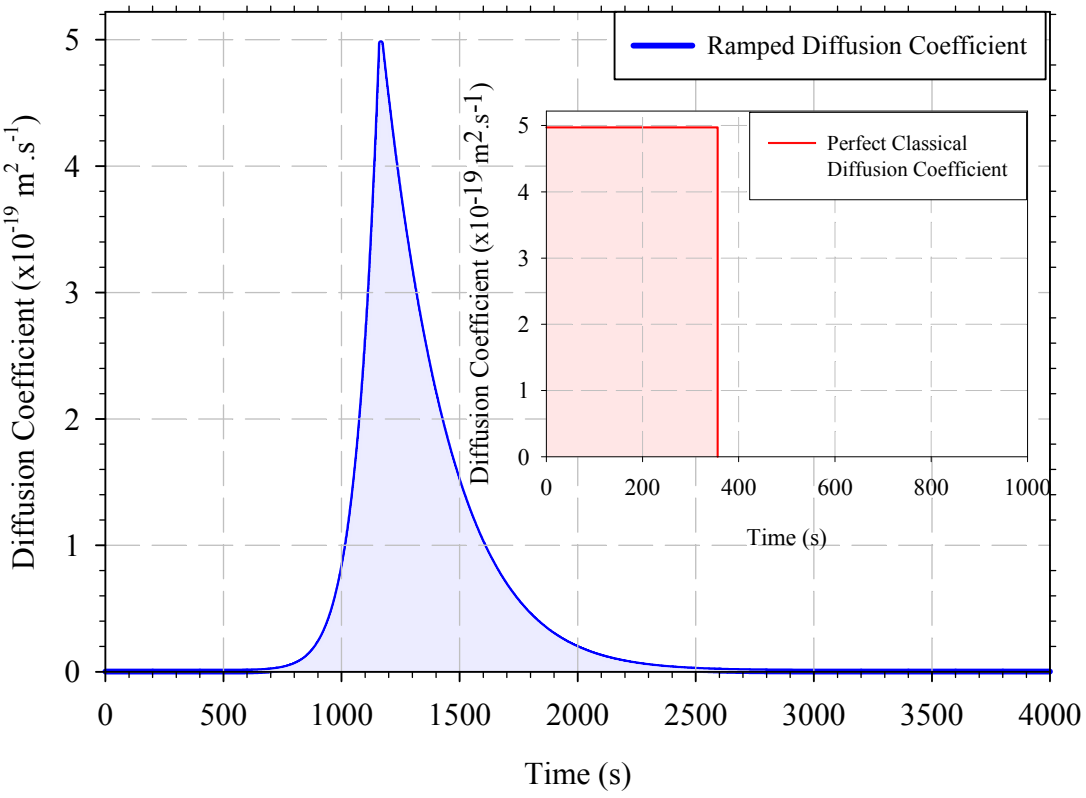

Figure 4.6: Representation of the change in the diffusion coefficient during a temperature ramp to a maximum of 400 °C. The area underneath the graph, which represents the amount of energy transferred to the sample, is shown as well. Included in the figure is an example of the equivalent perfect classical annealing diffusion coefficient as a function of time.

A perfect classical diffusion calculation can be performed with the maximum annealing temperature by simply changing the annealing time until the area underneath the curve (that represents the perfect classical annealing method) matches the area underneath the ramped curve, also shown in Figure 4.6. The amount of energy transferred to a sample during a perfect classical anneal will then equal the energy

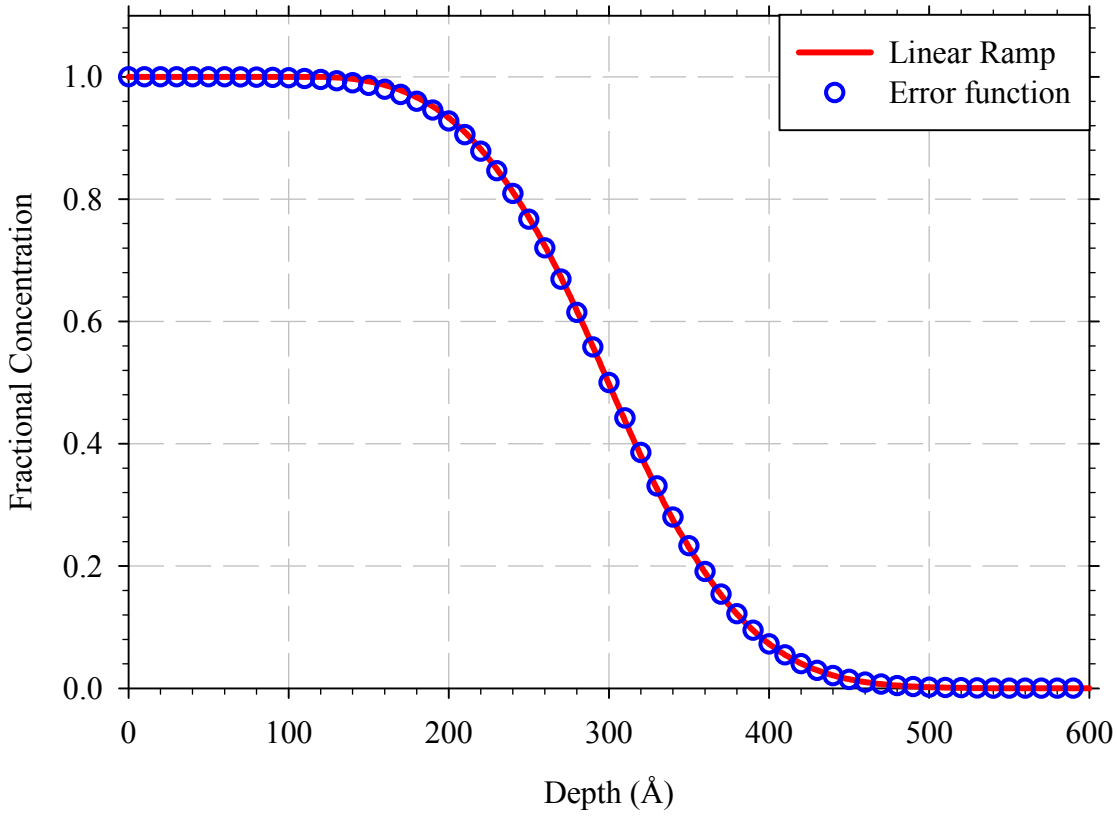

Figure 4.7: Comparison of diffusion profiles calculated from linear ramping and perfect classical heating.

This hypothesis was confirmed by performing a linear ramp diffusion calculation and comparing it to a perfect classical diffusion calculation. The perfect classical calculation accurately follows the linear ramp calculation, shown in Figure 4.7, confirming the hypotheses discussed earlier in this section. Using the method described above, one can analyse ramped diffusion profiles with the well established MRI model and extract diffusion parameters from the ramped data. Experimental data was analysed using the techniques described in this chapter as well as in the previous chapters. The setup used in the experimental study is described in the following chapter.

Chapter 5 – Experimental Setup

5.1 Introduction

To support the theoretical models described in the previous chapters, a number of experiments were done. This chapter deals with the preparation of samples used in this study and also discusses the annealing methods employed. Furthermore, the analysis method used in this study (Auger electron spectroscopy) is also briefly discussed and a description of the MRI analysis software used in the analysis is also given.

5.2 Sample Preparation

When studying diffusion of two different species, the choice of a substrate becomes a very important factor. An ideal substrate should not take part in the diffusion process nor should it chemically react with the material deposited on it. For this study, two types of substrates were used: glass and passivated silicon.

The glass substrates were used for the classical annealing part of the experiment and the passivated silicon for the temperature ramping part of the experiment. The surface of the glass substrate needed no chemical alterations as it is already passivated; the only drawback to using glass in conjunction with Auger electron spectroscopy is charging of the glass as a result of the incident electron beam.

For the temperature ramping part, single crystal silicon, orientation (100), was oxidized by wet oxidation at a temperature of 1000 ^{o}C for one hour, resulting in a SiO_2 layer with a thickness between 1 and 3 μm [47]. The oxide layer acts as a diffusion barrier, preventing any interaction between the silicon and the copper/nickel that will be deposited on the substrate.

Cu/Ni thin film samples were prepared by electron beam physical vapour deposition in an ultra high vacuum environment onto a passivated silicon (100) substrate (SiO_2), resulting in polycrystalline thin film layers. The nickel film was deposited at a rate of 1.3 Å.s^{-1} and had a thickness that varied between 800 Å and 1000 Å while the copper film was deposited at a rate of 3-5 Å.s^{-1} with a varying thickness used for the classical and linear annealing schemes. The emissivity current during the deposition of Ni was 160 mA and for Cu 60 mA. A schematic of the evaporation system is shown in Figure 5.1. The evaporation system was pumped to a base pressure of 9×10^{-6} Torr by a rotary vane and turbo molecular pump. The low pressure ensured that there was little contamination of the nickel and copper layers. The thickness of the deposited layers was monitored with an Inficon thickness monitor that uses the frequency response of a vibrating quartz crystal to determine the thickness of the deposited layer.

Figure 5.1: Picture of the electron beam physical vapour deposition system used during the course of this study.

5.3 Annealing – Classical Approach

The samples used in this section had a thickness that varied 2000 Å to 12000 Å. The samples were annealed in a temperature range of 250 ^{o}C to 450 ^{o}C for times varying between 36 minutes and 81 minutes, also in an ultra high vacuum environment. A complete list of annealing temperatures and times is listed in Table 5.1.

Sample Number	Annealing Time (s)	Annealing Temperature (^{o}C)
A1	250	2160
A5	275	2160
A6	300	2160
A7	350	2160
A8	325	2160
AR	-	-
B2	300	2940
B3	250	2940
B4	350	2940
B5	325	2940
B8	275	2940
BR	-	-
C1	275	3840
C2	325	3840
C3	350	3840
C4	300	3840
C8	250	3840
CR	-	-
D1	350	4860
D2	250	4860
D3	275	4860
D6	325	4860
DR	-	-

Table 5.1: Summary of annealing times and temperatures used for the classical annealing study

The annealing chamber is a custom built system with a carousel holder, allowing one to anneal multiple samples sequentially without breaking vacuum. The annealing system is shown in Figure 5.2.

A carousal is built into the annealing system which allows one to load several samples at once. The samples are placed on a ceramic boat and a magnetically controlled arm pushes the ceramic boat into and out of the oven.

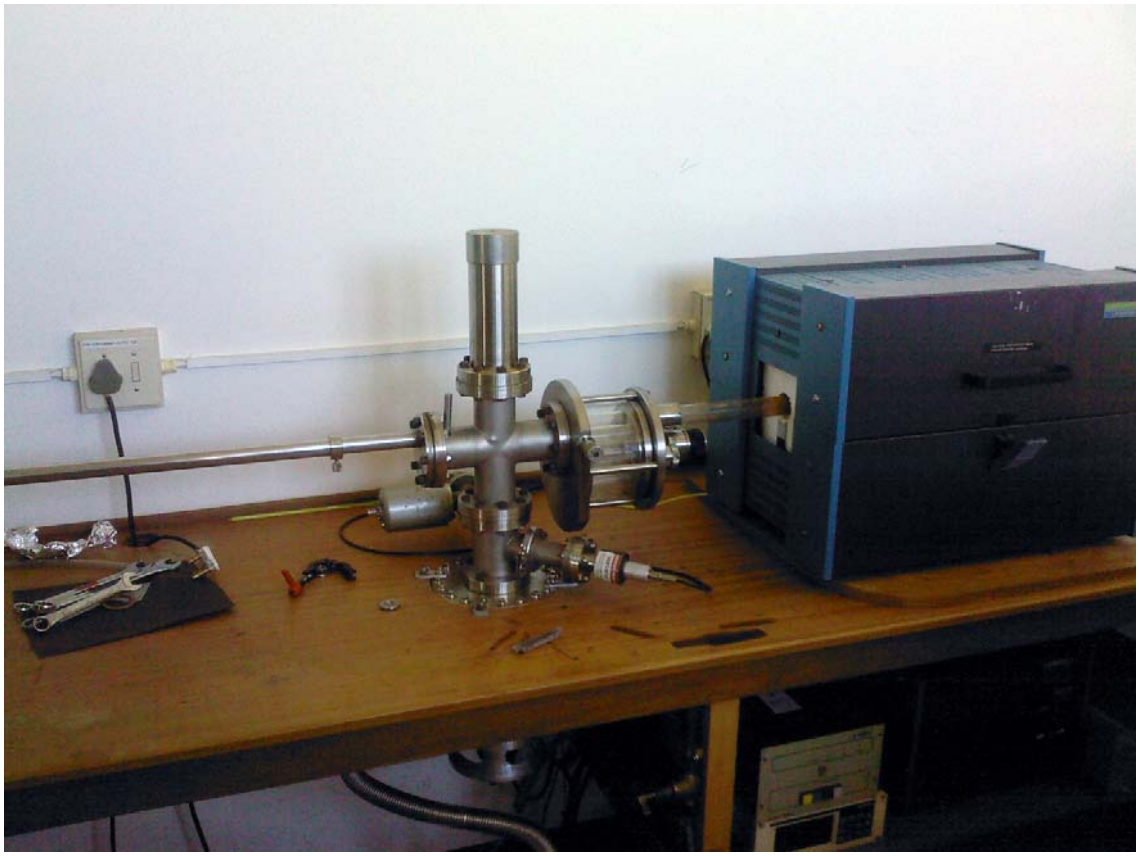

Figure 5.2: Picture of the custom built vacuum annealing system used during the course of this study.

5.4 Annealing – Ramping Approach

Samples were created with same procedure as mentioned in the previous section, the only difference being that a passivated silicon (100) substrate was used for the linear ramp samples. The nickel film had a thickness of 1000 Å while the copper film had a thickness of 6000 Å. Evaporation was performed in a vacuum with a base pressure of $<10^{-6}$ Torr.

For the linear annealing, another custom built heating unit was used. This unit is pictured in Figure 5.3.

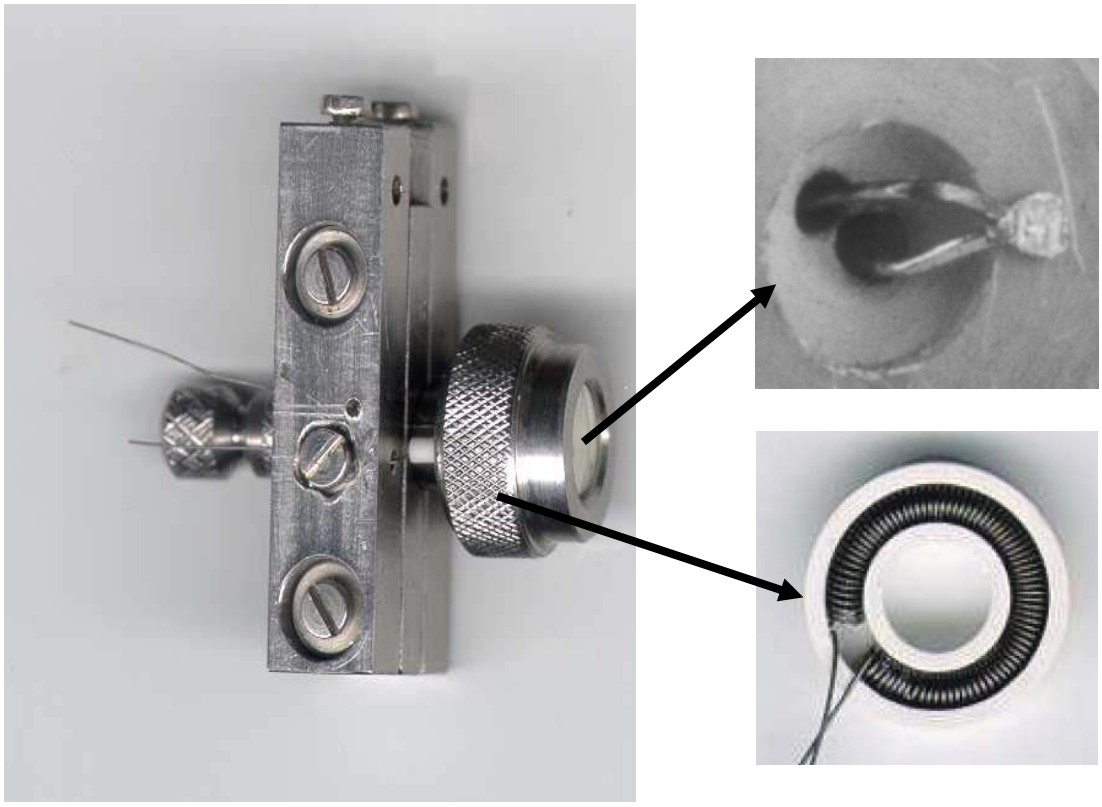

Figure 5.3: Heating unit built specifically for linear ramping measurements.

Part of the design specification of the heater included the ability to perform linear ramp annealing inside the UHV chamber of the Scanning Auger Microprobe. This allows one to monitor the surface of the sample while the annealing is taking place. The samples' temperature was measured by a Chromel/Alumel thermocouple in contact with the back of the sample. The temperature of the sample is computer controlled, with the computer connected to a temperature ramping control unit that adjusts the voltage and current that flows through the heater filament. Communication between the computer and the temperature ramping control unit is bi-directional, with the computer setting the sample temperature as well as reading the samples' temperature.

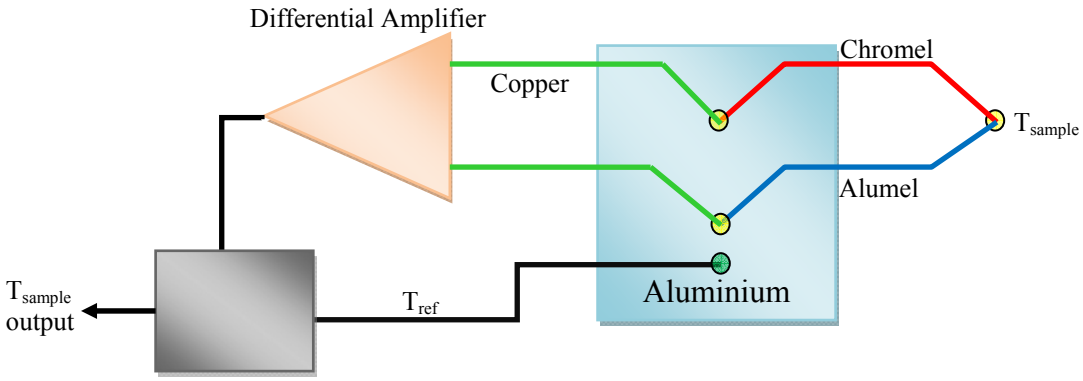

Figure 5.4: Schematic of the thermocouple connection used to measure a samples temperature.

Sample number	Number of Ramps	Maximum Temperature (^{o}C)
1, 8	1, 2, 3, 4, 5	350
6, 9	2, 3, 4, 6, 9	375
3, 4	1,2,3,4,5	400
7	1,2,3	450
2	1,2,3	500
10	1,2,3	550
11	1,2,3	450

Table 5.2: Summary of maximum temperatures used for linear ramping, as well as the number of ramps per sample.

To ensure accurate temperature readings from the thermocouple, a reference temperature is used as a control temperature. The reference temperature is obtained from a unit that contains a solid aluminium block, heated to 35 ^{o}C. The connection of the thermocouple to the sample, reference temperature block and control unit, is shown in Figure 5.4.

Samples were then heated at a controlled rate of 0.3 $^{\circ}C.s^{-1}$ and cooled at controlled rate of -0.1 $^{\circ}C.s^{-1}$ to maximum temperatures ranging from 350 $^{\circ}$C to 500 $^{\circ}$C, except sample 10 which was heated at 1 $^{\circ}C.s^{-1}$ and sample 11 that was heated a rate of

$0.6\,^{\circ}C.s^{-1}$ and cooled at $0.2\,^{\circ}C.s^{-1}$. Information regarding the number of ramps and the maximum temperatures used for ramping is shown in Table 5.2

5.5 Auger Measurements

Measurements were done on a Physical Electronics 590 Scanning Auger Microprobe. The system has been modified over the years and currently consists of the following units:

- Ion pump capable of pumping to a pressure of $<10^{-8}$ Torr.
- Physical Electronics Electron Gun (PHI Model 18-085).
- Single Pass Cylindrical Mirror Analyser (CMA).
- Physical Electronics Auger System Control (PHI Model 11-055) which controls the voltage on the plates of the CMA, while the control unit is connected to a computer that can set the desired CMA voltage.
- Physical Electronics Electron Multiplier Supply (PHI Model 20-075).
- Physical Electronics Lock-in Amplifier (PHI Model 32-010).
- Perkin Elmer Ion Gun (11-065).

The Scanning Auger Microprobe system is shown in Figure 5.5.

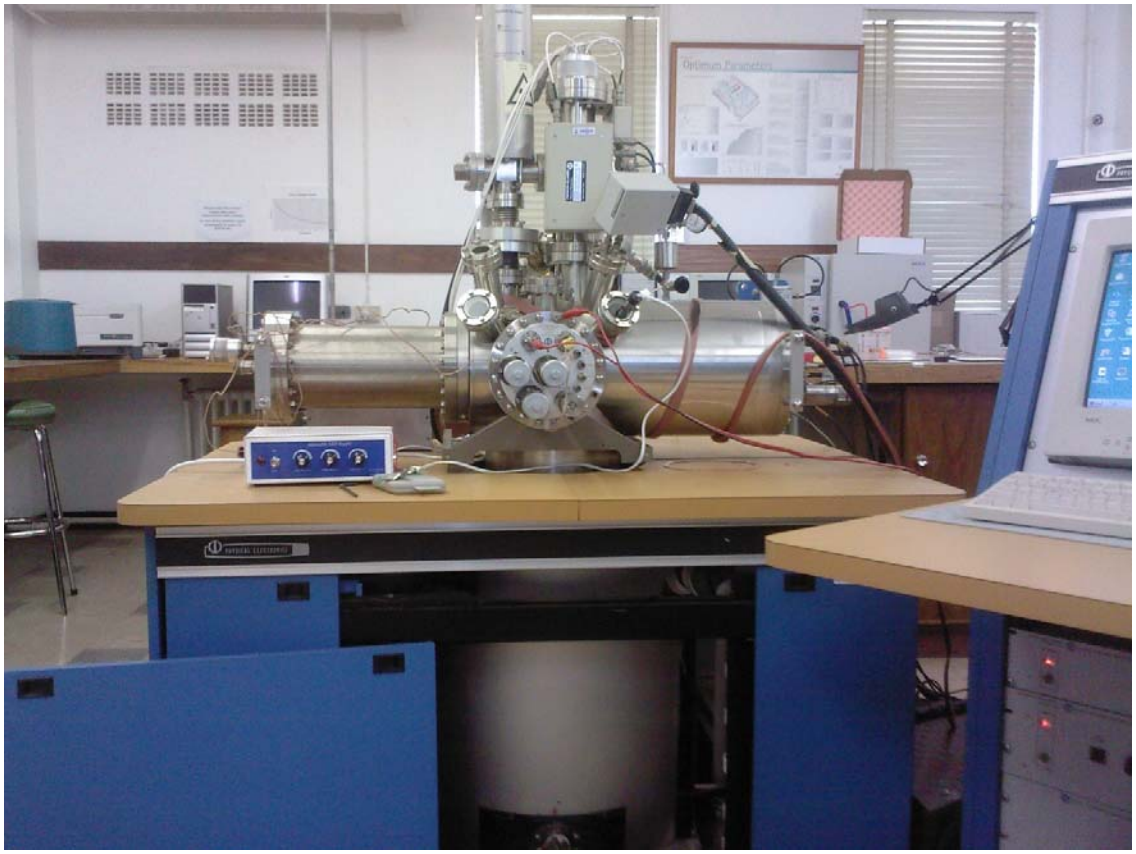

Figure 5.5: The PHI 590 SAM system used during this study.

The parameters used during this study are shown in Table 5.3. Before any measurements were made, the system was turned on and allowed to stabilise for one hour. The electron gun filament and ion gun filament were de-gassed by slowly turning up the current flowing through the filaments. Once the system was fully de-gassed and the base pressure stabilised, the distance between the sample and the CMA was adjusted until the elastic peak was at the correct (2000 eV) position. Argon gas was leaked into the ion gun and the ion beam was then positioned so that the beam strikes the sample at the same position that the electron beam strikes the sample. The system was then calibrated using a copper standard after which the system was ready to use.

	Parameter	*Value*
Electron Beam	Beam current	7.5×10^{-7} A
	Emission current	≤ 0.1 mA
	Voltage (elastic peak)	2 kV
	Voltage (measuring)	5 kV
Argon ion gun	Beam current (no raster)	1.4×10^{-7} A
	Beam current (raster)	1.25×10^{-8} A
	Emission current	25 mA
	Argon beam voltage	2 kV
	Raster size	3×3 mm
Measurement settings	Scan rate	5 eV.s^{-1}
	Modulation voltage	4 eV
	Sensitivity	$40\times$
	Time constant	0.1 s
	Photo-multiplier voltage (elastic peak)	0.85 keV
	Photo-multiplier (measuring)	1.35 keV
Peaks monitored	Si	
	Cu (low energy) Ni (low energy)	$40\rightarrow120$ eV
	Cu (high energy) Ni (high energy)	$650\rightarrow980$ eV
	O	$480\rightarrow540$ eV
	C	$245\rightarrow300$ eV

Table 5.3: Settings used for measurements taken on the PHI 590.

An Auger scan for a Ni/Cu reference sample is shown in Figure 5.6. The data is captured in differential mode which simplifies analysis later on.

Another custom developed software package was used during the analysis of the Auger peaks. The software allows the user so select the area in which the maximum and minimum peak positions are located and then automatically reads all the Auger peak files to construct a depth profile.

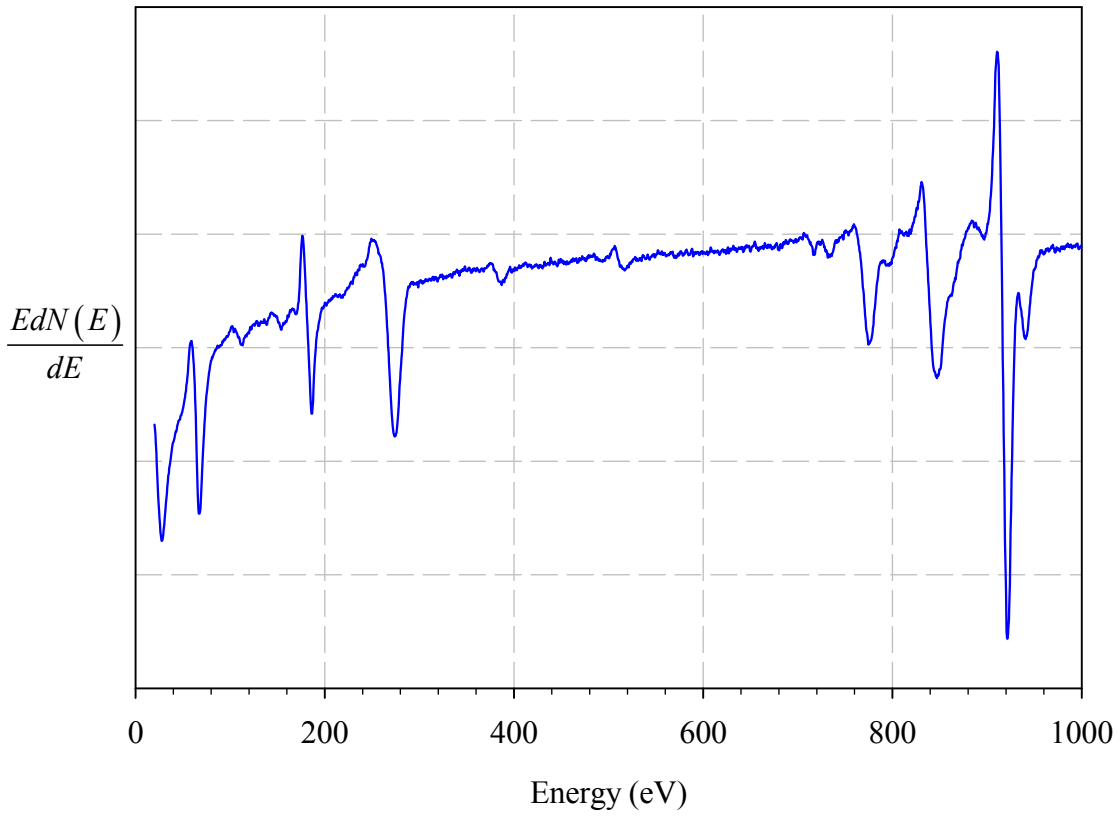

Figure 5.6: Auger scan of from 20 eV to 1000 eV of a copper standard before sputtering cleaning of the surface.

A depth profile of a reference sample of Cu/Ni is shown in Figure 5.7. This depth profile was obtained using the parameters listed in Table 5.3. Also, the sample depth profile has not been converted to atomic concentration and the time scale has not been converted to depth. Both of the aforementioned points are dealt with in subsequent sections.

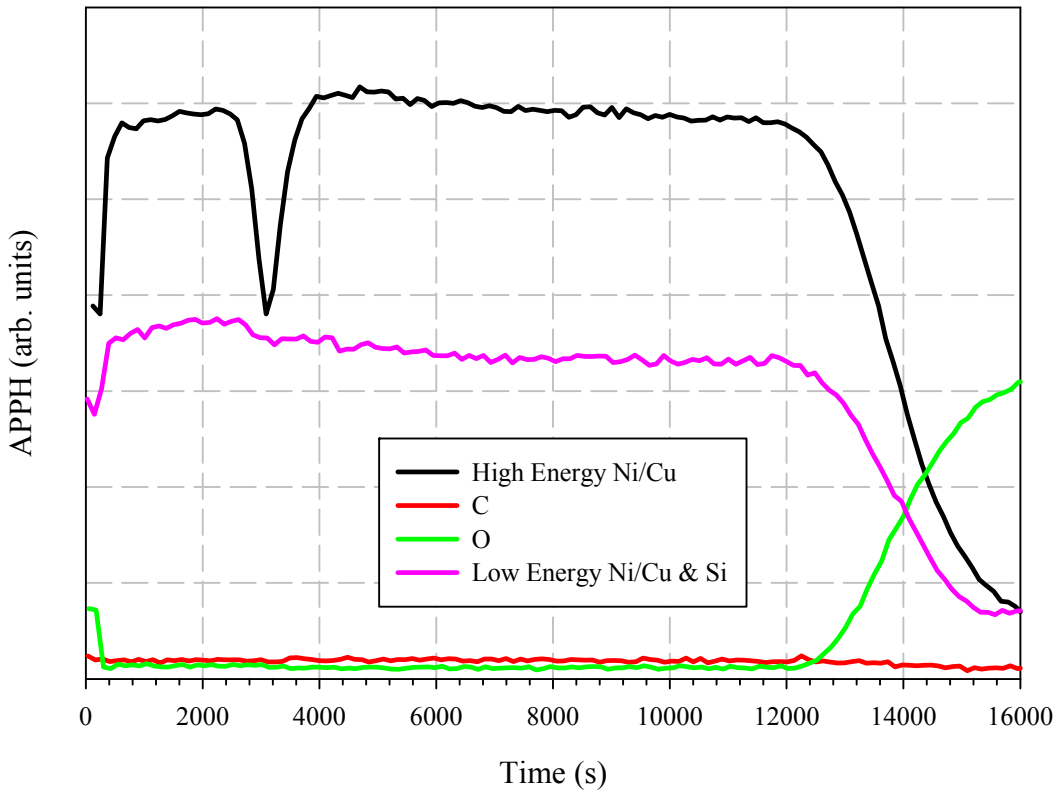

Figure 5.7: Example of an as measured depth profile taken with the measurement parameters listed in Table 5.3.

One apparent problem with the depth profile in Figure 5.7 is the lack of a clear boundary between the nickel and copper layers. The root cause of this problem is the overlapping of the Auger peaks used during quantification. This problem is also dealt with in the next section.

5.6 Auger Quantification

In many Auger experiments, overlapping of the Auger electron energy peaks occurs. In such a situation, quantitative information cannot be readily extracted from the measured data. In order to definitively quantify the measured spectrum, the contribution of the various elements to the measured spectrum must be determined. This specific problem is addressed in the next section.

5.6.1 Separation of overlapping Cu/Ni peaks

The Ni/Cu system studied has a unique Auger energy spectrum both on the lower end and the higher end of the scale. The low energy peaks are very difficult to separate from one another and will not be considered in this study.

The high energy peaks of both copper and nickel also overlap, but the overlap is not as pronounced as in the low energy peaks. When analysing a system that contains both copper and nickel, quantification is hampered by the overlapping energy peaks. This overlap is shown in Figure 5.8.

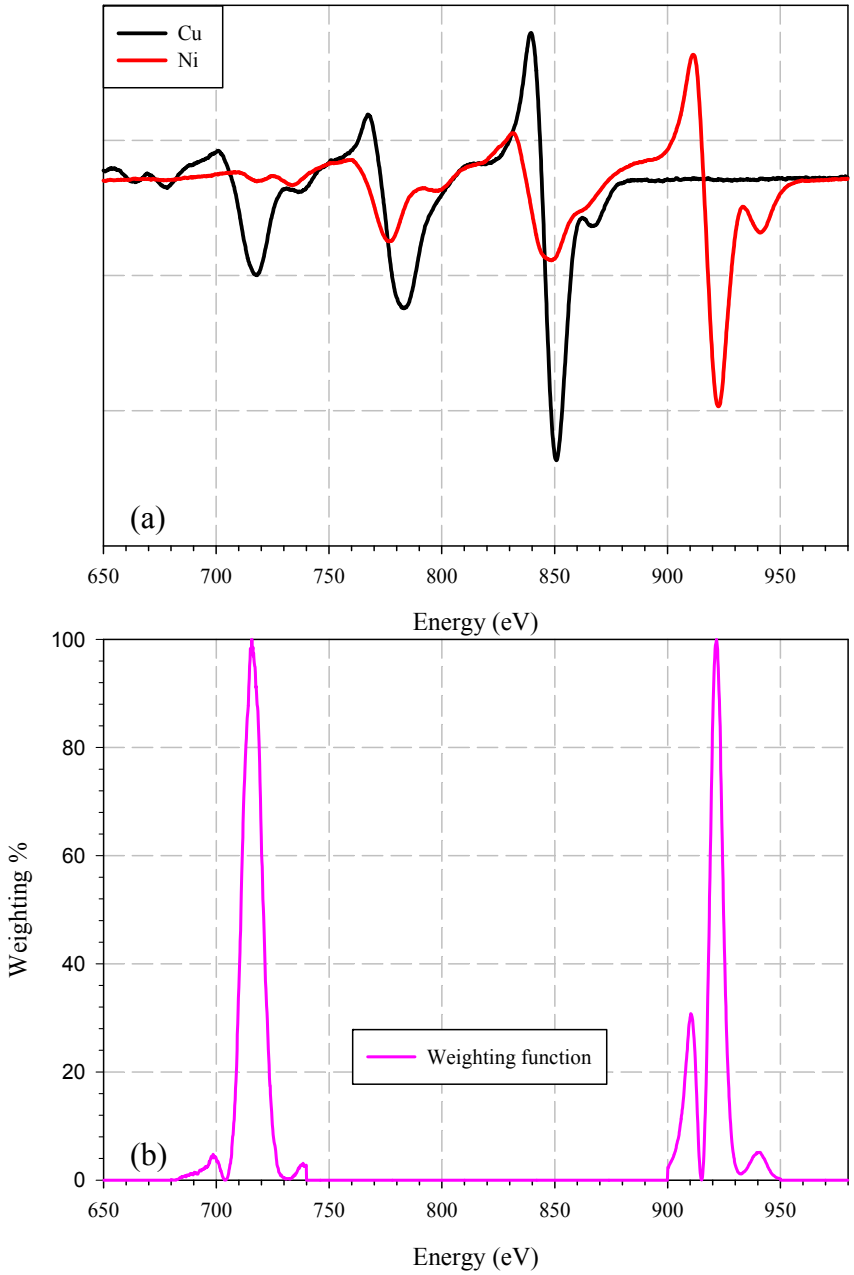

Figure 5.8: High energy Auger peaks of copper and nickel (a) as well as the weighting function (b) used in the Linear Least Squares technique.

A clear overlap in peak shapes is visible in Figure 5.8 and this complicates quantification as the contribution of a single element cannot be determined without determining what the contribution of each element is to the measured spectrum. One method of determining each element's contribution to the measured signal is the

Linear Least Squares (LLS) technique. The LLS method uses standards of pure elements to determine the contribution of each element to a measured spectrum. Working from the supposition that the measured spectrum b of N channels can be represented by a linear combination of the K standard spectra, the measured spectrum b is given by [48]

$$\mathbf{A}\mathbf{x} = b \tag{5.1}$$

where **A** is a $N \times K$ matrix with the standard spectra of the contributing elements as columns and **x** is a vector with length **K** containing the concentrations of the contributing elements. The Auger spectrums shown in Figure 5.8 shows a distinct difference between the copper and nickel spectra, specifically the high energy peak of copper does not overlap with any nickel peaks. Also, the low energy nickel peak has a distinct shape that also differs significantly from copper spectrum. If a weighting function is introduced that removes all contributions except the high energy peak of copper and the low energy peak of nickel, quantification becomes considerably easier. Such a weighting function **W** (shown in Figure 5.8) can be added to (5.1), which results in

$$\mathbf{W}\mathbf{A}\mathbf{x} = \mathbf{W}b \tag{5.2}$$

with a solution of the form

$$\mathbf{x} = \left(\mathrm{A}^T\mathbf{W}\mathbf{A}\right)^{-1}\left(\mathbf{A}^T\mathbf{W}\mathbf{b}\right) \tag{5.3}$$

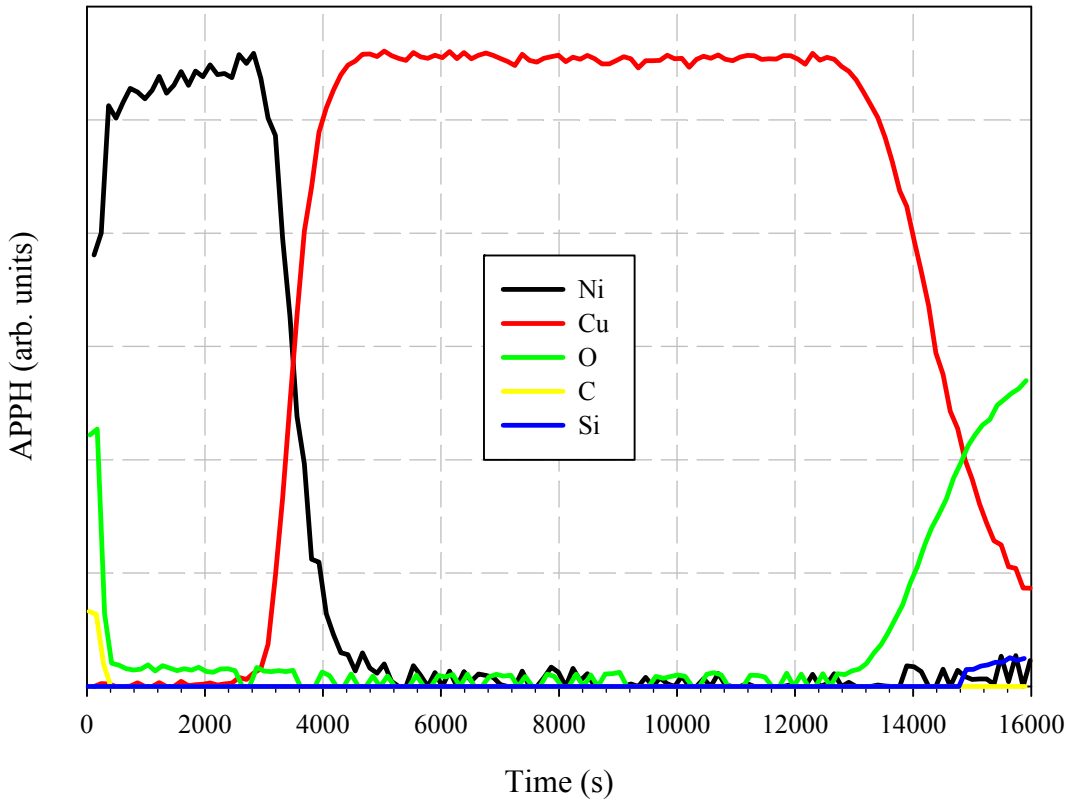

Figure 5.9: Example depth profile with the overlapping peaks separated with the LLS method described in the text.

with the superscripts *T* representing the transpose and -1 the inverse. The technique described above is used throughout this study. As an example, Figure 5.7 was analysed with the LLS technique and the results are shown in Figure 5.9.

5.6.2 Concentration Scale Calibration

Further analysis of Figure 5.9 requires conversion of the APPH axis to a concentration scale, i.e. the depth profile must be quantified. If the sample under investigation is uniform, quantification is performed by comparing the measured signal intensities of a reference sample with the measured signal intensities of the sample under

investigation. This is approach is called the relative sensitivity factors (RSF) approach. For a multi-component system, the concentration of any particular element can be calculated from [49, 50]

$$C_i = \frac{I_i / I_i^0}{\sum_{j=i}^{n} I_j / I_j^0}. \tag{5.4}$$

where I_i^0 is the measured spectrum of the pure reference sample, I_i is the measured spectrum of the sample under investigation and the summation is done over all elements (n) in the sample.

To compensate for backscattering and matrix effects, a matrix factor is incorporated into equation (5.4), resulting in [50, 51]

$$C_i = \frac{F_{ij} \cdot I_i / I_i^0}{\sum_{j=i}^{n} F_{ij} \cdot I_j / I_j^0}, \tag{5.5}$$

The matrix factor for a binary system composed of elements A and B has the form [51, 52]

$$F_{ij} = \left[\frac{1 + r_A(E_A)}{1 + r_B(E_A)}\right]\left(\frac{a_B}{a_A}\right)^{3/2} \tag{5.6}$$

where a_A is the atomic size of element *A* and a_B is the atomic size for element *B* and $r_A^{E_A}$ and $r_B^{E_A}$ is the backscattering factor for element *A* and *B* described by Shimizu's [52, 53] equation

$$r = 1 + \left(0.462 - 0.777Z^{0.2}\right)U_0^{-0.32} + \left(1.15Z^{0.2} - 1.05\right) \tag{5.7}$$

where Z is the atomic number for an elemental solid and U_0 is the ratio of the primary-electron energy to the threshold energy for inner-shell ionization of the core level responsible for the Auger transition.

Equation (5.6) is only valid for a binary system, and for a multi-component system, average values for the atomic numbers must be used [51]. The inherent problem with the aforementioned statement is that the composition is not known when the quantification takes place. One way to overcome this problem is to use equation (5.4) as a first step to determine the elemental concentrations and use these concentrations in the calculation of the average atomic numbers [51].

During this study, equation (5.5) was used extensively to convert the APPH of the measured profiles to concentration, an example of which is given in Figure 5.10. The next section discusses the conversion of the sputtering time to sputtering depth.

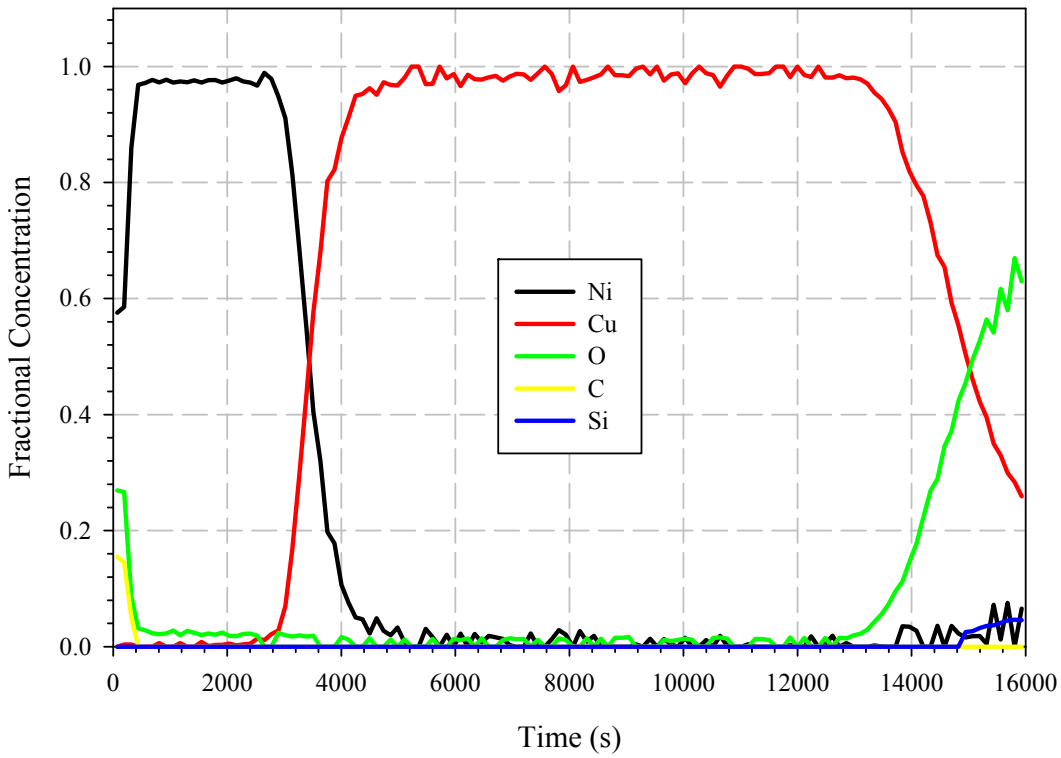

Figure 5.10: Reference sample with the APPH axis converted to concentration.

5.6.3 Depth Scale Calibration

Following on the previous sections, the final part of the quantification of a depth profile involves the conversion of the sputtering time to depth. If one assumes that the primary ion current density is constant, then the sputtering time is proportional to the ion dose density [35]. From this relation it is possible to determine the sputtered depth z_1 at sputtering time t from the instantaneous sputtering rate $\dot{z} = \frac{dz}{dt}$, obtained from

$$z(t_1) = \int_0^h \dot{z}(t)\,dt \tag{5.8}$$

where $\dot{z}$ is represented by

$$\dot{z} = \frac{j_p Y_m}{Ne} \tag{5.9}$$

with $j_p \left(\text{A.m}^{-2}\right)$ the ion current density, Y_m the sputtering yield, N the atomic density and e the elementary charge. If one assumes a constant sputtering yield and atomic density, the instantaneous sputtering rate is constant, and hence the average sputtering rate is given by [35]

$$z = \dot{z}t \,. \tag{5.10}$$

Since the sputtering yield and atomic density cannot be determined with sufficient accuracy, other methods are employed to determine the sputtered depth after a certain sputtering time. One method of overcoming this problem is to measure the crater depth and determining the interface location of single or multilayer structures. A further problem that complicates the conversion to depth is that the sputtering rate changes as the composition of the sample changes. This will necessitate that the instantaneous sputtering rate be measured in situ during sputtering, either by laser interferometry or determination of the mass of the sputtered material [35].

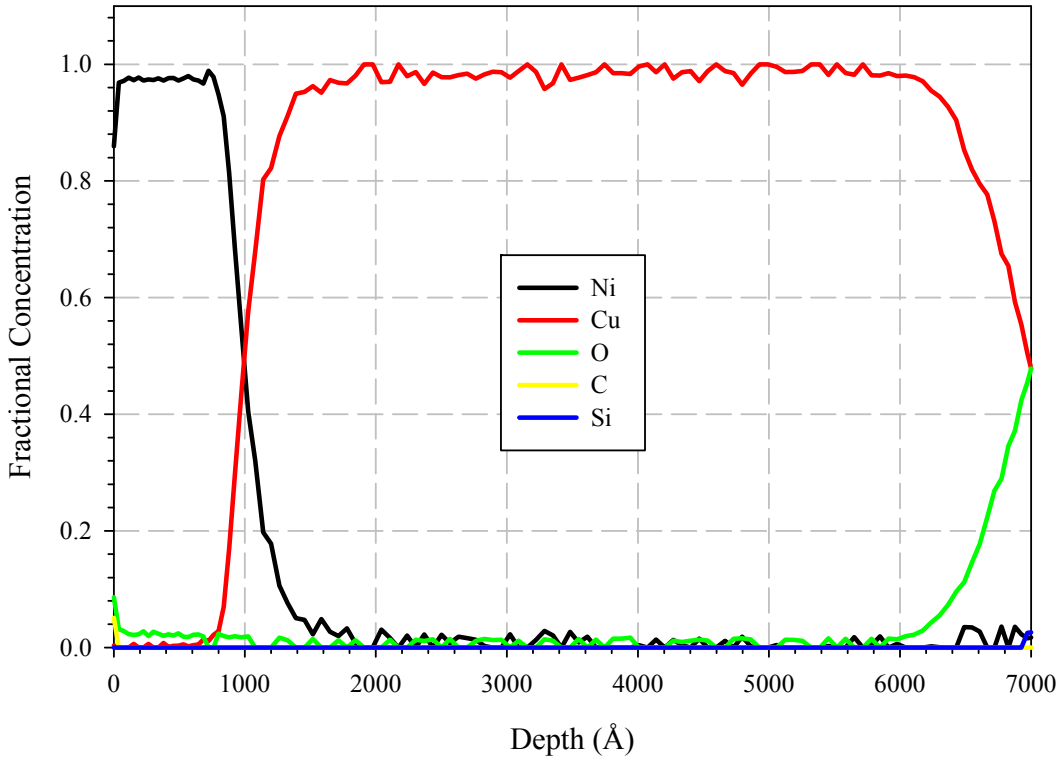

Figure 5.11: Fully quantified depth profile.

In most situations in situ monitoring is not available and the sputtering rate can be estimated if one assumes a linear dependence with composition. For a binary system (A, B), the sputtering rate can be estimated with

$$\dot{z}(t) = \dot{z}_A C_A + \dot{z}_B C_B \tag{5.11}$$

where $\dot{z}_A$ and $\dot{z}_B$ is the sputtering rate for element A and B, and C_A and C_B is the concentration of element A and B respectively. Using equation (5.11), one can convert the sputtering time to depth if the thickness of the layers comprising the sample is known. Using the technique described above, the original depth profile shown in Figure 5.9 has been converted to a quantified profile, shown in Figure 5.11.

5.7 MRI Analysis software

After a depth profile has been quantified as described in the above sections, the depth profiles were reconstructed with the MRI model. To accomplish this, a software package was written to perform the reconstruction. A screen capture of the software is shown in Figure 5.12.

By adjusting the mixing width and surface roughness parameters, a MRI fit is obtained by comparing the calculated profile with the measured profile. For a detailed discussion of the MRI analysis technique, the reader is referred to ref. [36]. As an example, a reference profile was analysed with the MRI model and the result is shown in Figure 5.13.

The next chapter documents the experimental results and includes a discussion of the results.

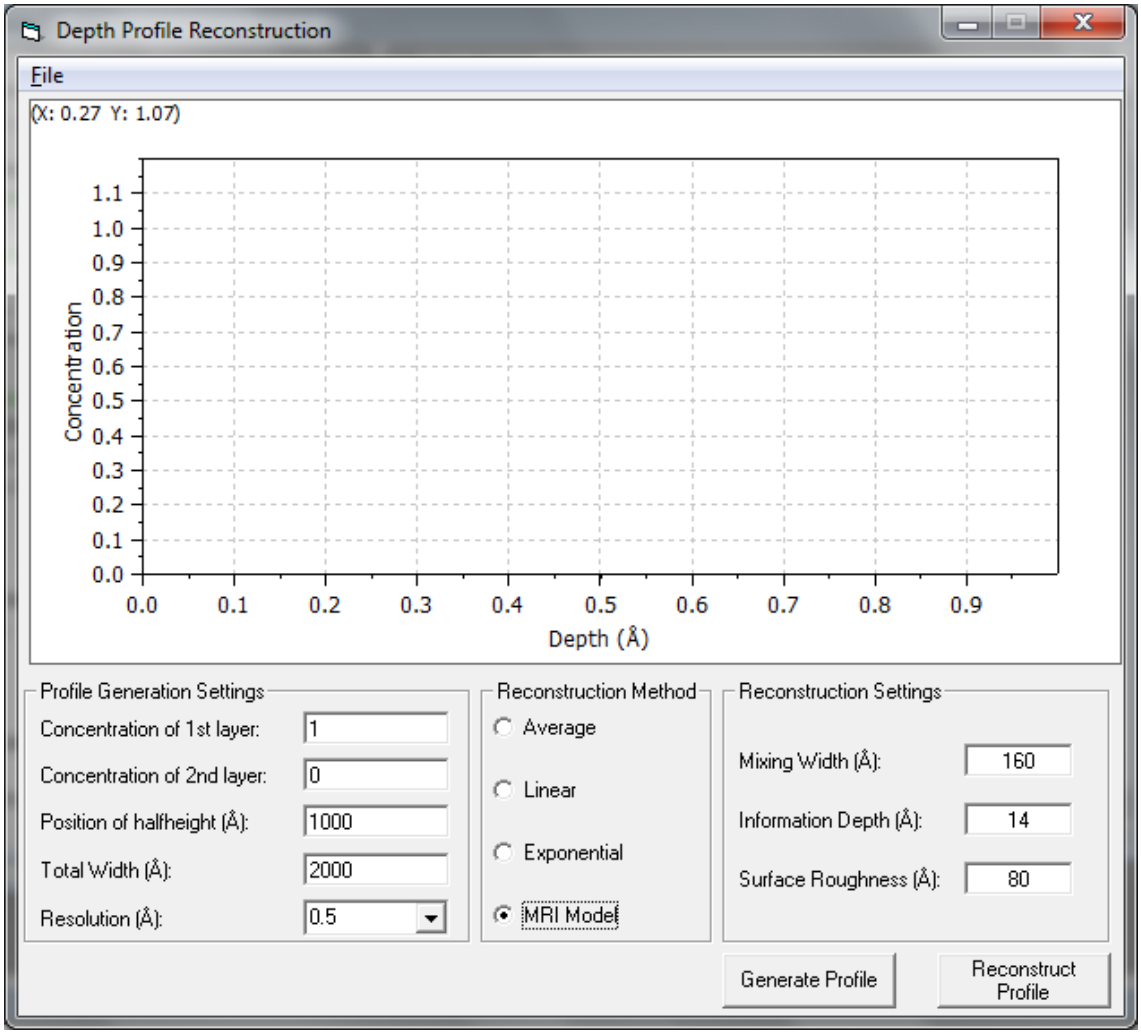

Figure 5.12: Graphical user interface of the software used for the MRI fits.

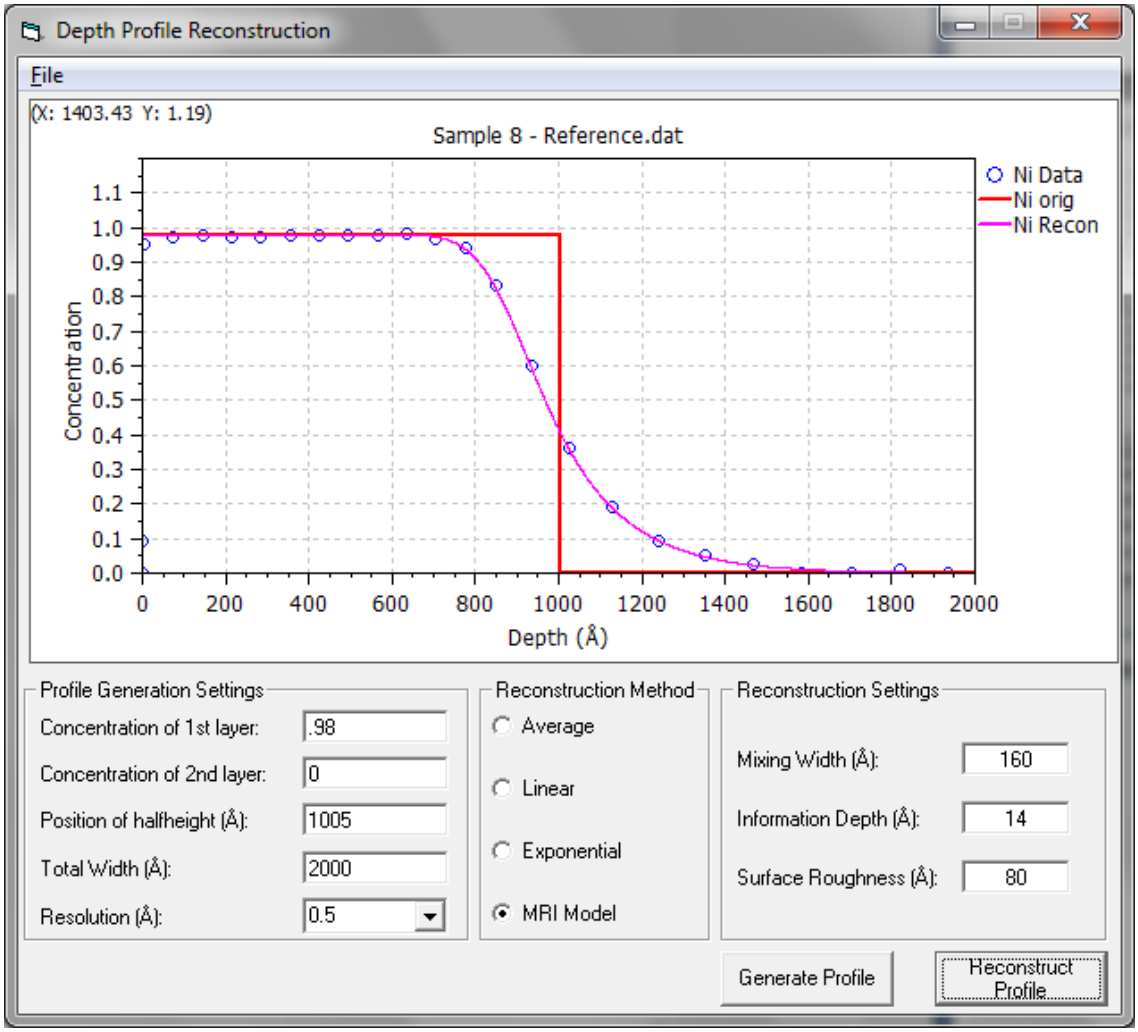

Figure 5.13: Example MRI fit to a reference depth profile.

Chapter 6 – Results and Discussion

6.1 Introduction

This chapter documents the results obtained over the duration of this study. As in the previous chapter, the classical annealing approach is discussed first, followed by the linear ramping approach. Finally a comparison is made between the results obtained from the classical heating approach and the linear ramping approach.

For the purposes of this study, only the diffusion coefficient of Ni in Cu will be determined as the focus is on the development of a new annealing method and the effect of annealing on the extracted diffusion coefficient. If one desires to obtain the diffusion coefficient of Cu in Ni, the exact same process of analysis described in this chapter and previous chapters can be used.

6.2 Diffusion coefficient of Ni in Cu – Classical Heating

The best fit MRI fit parameters obtained for all the samples used in this part of the study are listed in Table 6.1. An example of the MRI fit obtained for several experimentally measured depth profiles is shown in Figure 6.1, where the solid line indicates the MRI fit.

Sample Number	Temperature (^{o}C)	Mixing Width (nm)	Information Depth (nm)	Surface Roughness (nm)
A1	250	40	1.3	9.7
A5	275	40	1.3	10.4
A6	300	40	1.3	11.1
A7	350	40	1.3	20.5
A8	325	40	1.3	13.8
AR	-	40	1.3	9.6
B2	300	40	1.3	11.3
B3	250	40	1.3	.
B4	350	40	1.3	21.5
B5	325	40	1.3	16
B8	275	40	1.3	10.9
BR	-	40	1.3	9.6
C1	275	40	1.3	11.1
C2	325	40	1.3	18.5
C3	350	40	1.3	26
C4	300	40	1.3	12
C8	250	40	1.3	9.75
CR	-	40	1.3	9.6
D1	350	40	1.3	27
D2	250	40	1.3	9.85
D3	275	40	1.3	11.4
D6	325	40	1.3	19
DR	-	10	1.3	9.6

Table 6.1: Best fit surface roughness and mixing width obtained for the different samples.

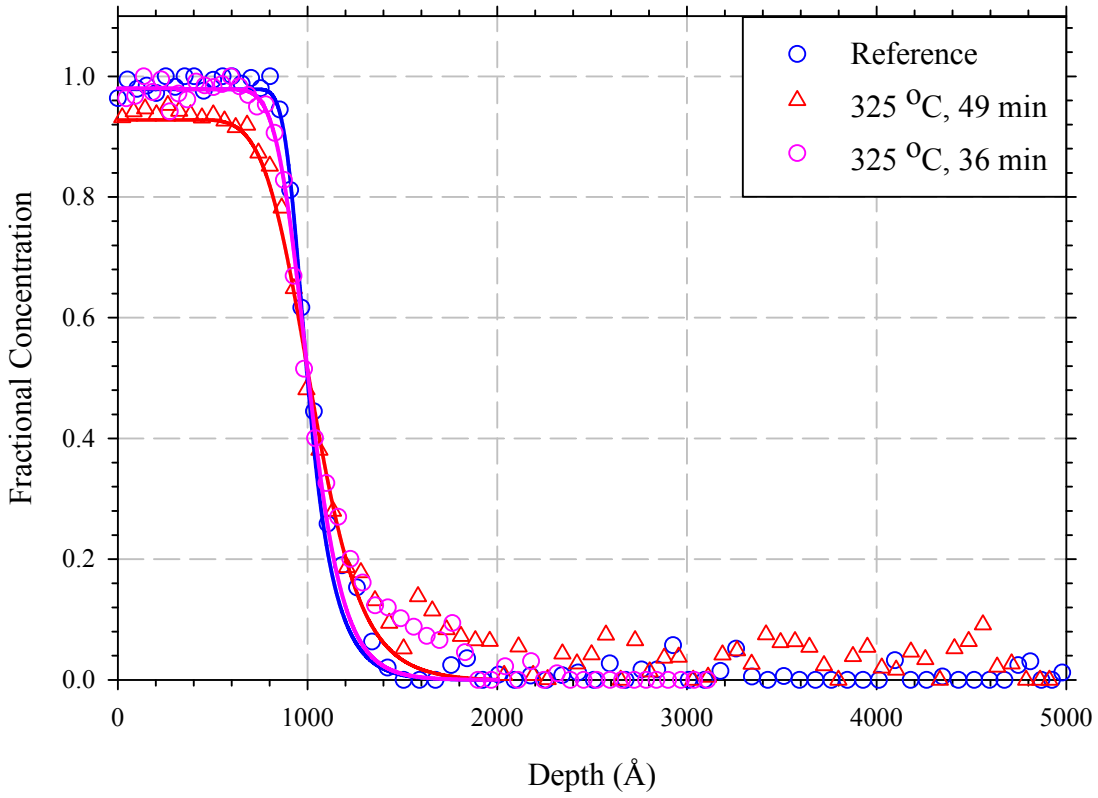

Figure 6.1: Example of experimental data and MRI fit.

As mentioned in Chapter 3, equation (3.13) is used to determine the diffusion coefficient from the surface roughness parameter of the MRI model. For this study, several samples were annealed at the same temperature, but for different times. One can then calculate the diffusion coefficient for each of the samples in the aforementioned situation using equation (3.13). However, since the Arrhenius formula has a temperature factor, one must obtain a single diffusion coefficient for **each** temperature that was used for annealing. There are two possible methods of obtaining the diffusion coefficient from multiple samples annealed at the same temperature. The first is to simply use the average diffusion coefficient of all the samples annealed at a particular temperature, obtained from a direct solution of equation (3.13).

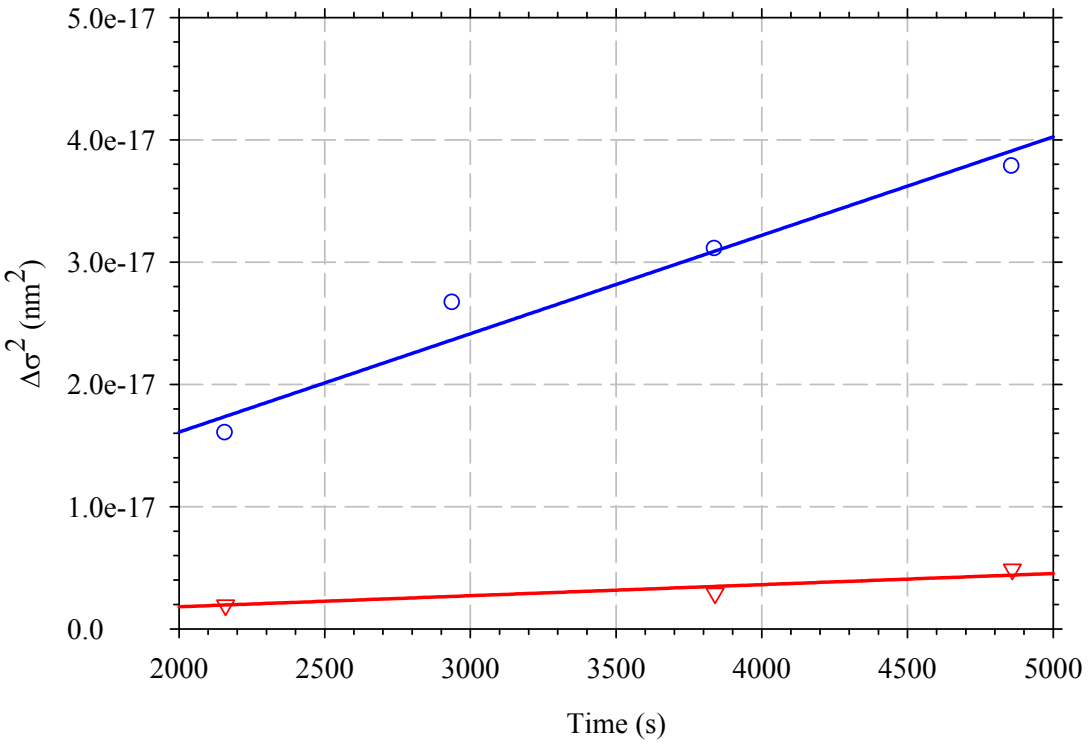

Figure 6.2: Best fit MRI parameters for 250 °C and 275 °C.

This introduces mathematical errors, and is not the most accurate method of analysis. The second method involves constructing graphs of $\Delta\sigma^2$ vs. time, shown in Figure 6.2 and Figure 6.3. Since equation (3.13) implies a linear relationship between the change in surface roughness and time, linear regression can be used to determine the diffusion coefficient for a particular annealing temperature. The y-axis intercept is zero and the slope of the resulting regression line is equal to $2D$, with D the diffusion coefficient, resulting in a diffusion coefficient for each annealing temperature. These diffusion coefficients are then plotted on an Arrhenius graph from which the diffusion coefficients can be determined, shown in Figure 6.4.

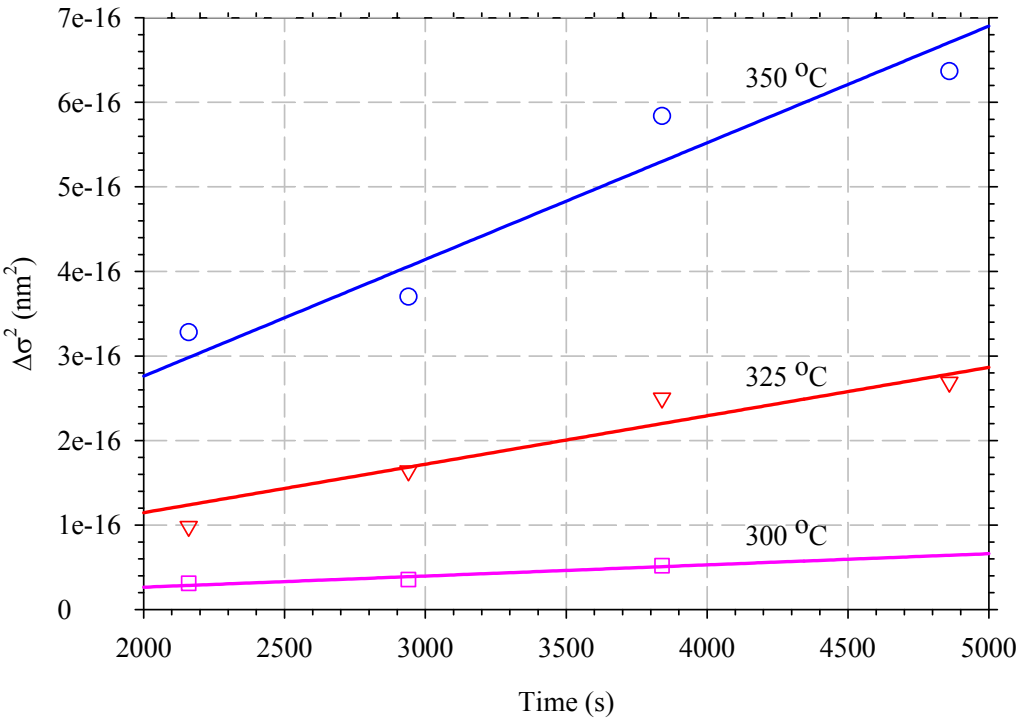

Figure 6.3: Best fit MRI parameters for 300 °C, 325 °C and 350 °C.

The pre-exponential frequency factor, D_0, and the activation energy, Q, is obtained by rewriting the diffusion equation (2.4) in the form

$$y = mx + c \tag{6.1}$$

which describes the straight line in Figure 6.4.

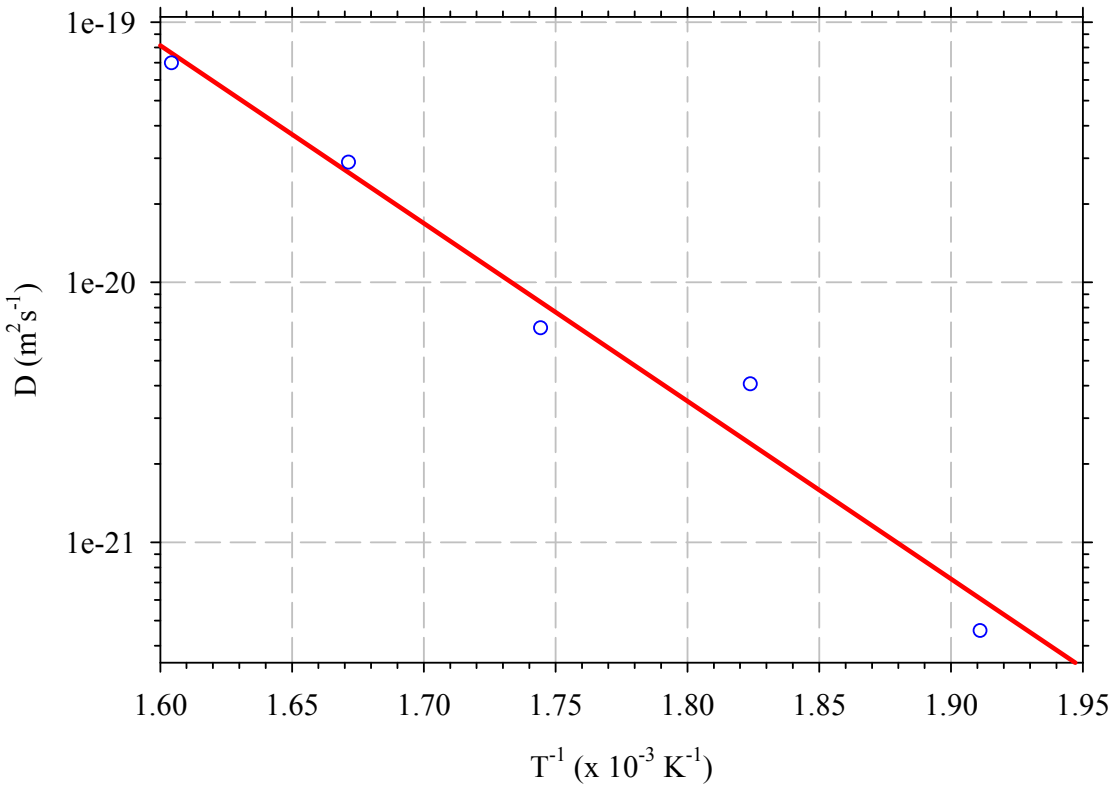

Figure 6.4: Arrhenius graph of the diffusion coefficients obtained from the MRI model fits.

The resultant equation has the form

$$\ln D = \left(-\frac{Q}{R}\right)\frac{1}{T} + \ln D_0 \tag{6.2}$$

where $-\frac{Q}{R}$ is equivalent to the gradient m and $\ln D_0$ is equivalent to the intercept c.

The pre-exponential factor and activation energy obtained from Figure 6.4 and equation (6.2) are listed in Table 6.2.

Source	D_0 $\left(m^2.s^{-1}\right)$	Q $\left(kJ.mol^{-1}\right)$
Classical Annealing	6.48×10^{-9}	130.5
Ref. [54]	2×10^{-5}	228.7
Ref. [55]	2.6×10^{-10}	133.1
Ref. [56]	6.93×10^{-7}	90.4
Ref. [57]	1.4×10^{-14}	106.1
Ref. [58]	4.9×10^{-13}	103.2

Table 6.2: Diffusion parameters obtained in the present work and from literature.

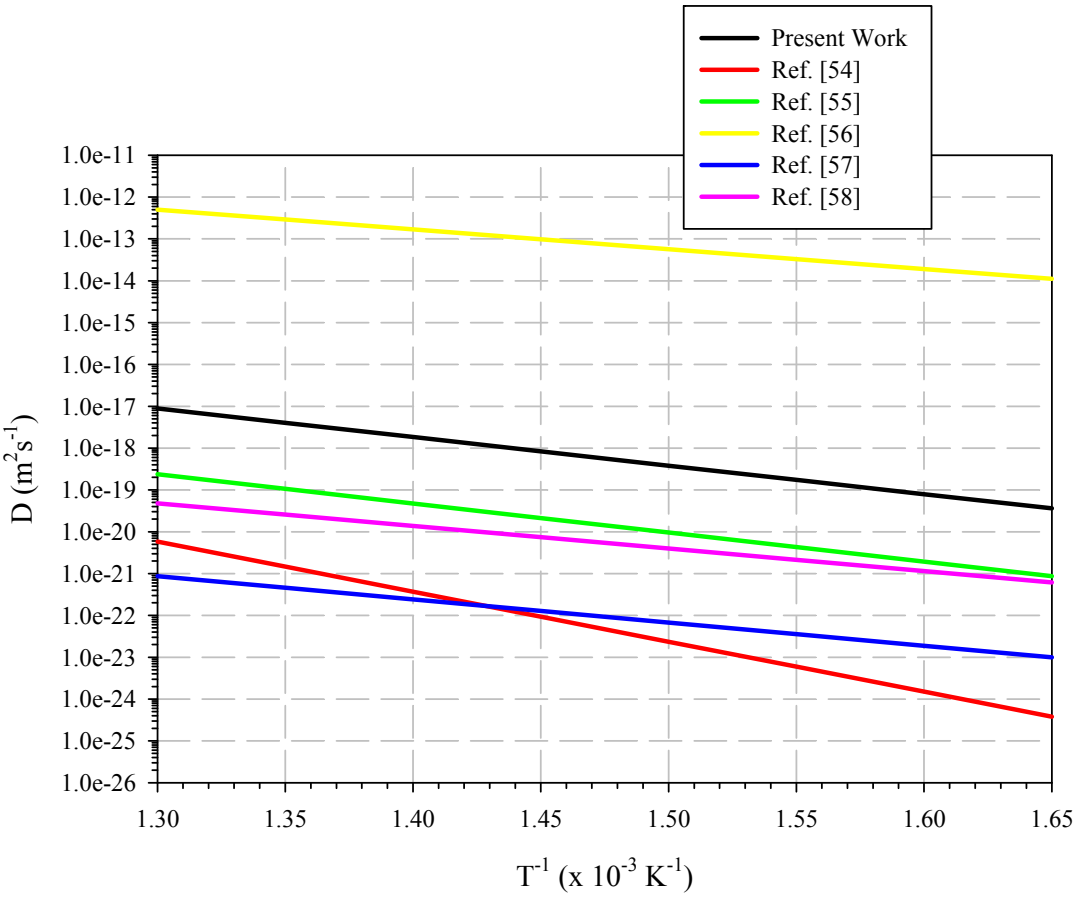

Figure 6.5: Arrhenius graph constructed from the diffusion parameters listed in Table **6.2**.

Along with the diffusion parameters obtained in this study, a number of literature values are also listed in Table 6.2 and these values are plotted in Figure 6.5. The large spread of values listed in Table 6.2 can be attributed to the varying conditions of preparation that were used to create the samples.

As an example, ref. [54] used a single crystal to determine the diffusion parameters, while the other investigators used polycrystalline materials. Rammo, et. al. [58] investigated the influence of the preparation conditions on diffusion and concluded that the preparation technique used to create a sample plays an important role in the type of diffusion observed. Different researchers will therefore obtain different results as the microstructure inside a sample depends, among others, on the substrate structure and the thickness of the layer [59].

To eliminate the variability of the sample composition, all the samples were created the same way, as described in the previous chapter. This includes the samples used for the linear ramping segment which follows in the next section. Since the method of creation of both sets of samples (linear and classical) is the same, the sample composition will be the same and this allows a direct comparison between the diffusion coefficients obtained from classical annealing and linear ramping.

The next section describes the extraction of diffusion coefficients from linearly ramped samples.

6.3 Diffusion Coefficient of Ni in Cu – Linearly Ramped Heating

An example of the MRI fits to linearly ramped data is shown in Figure 6.6.

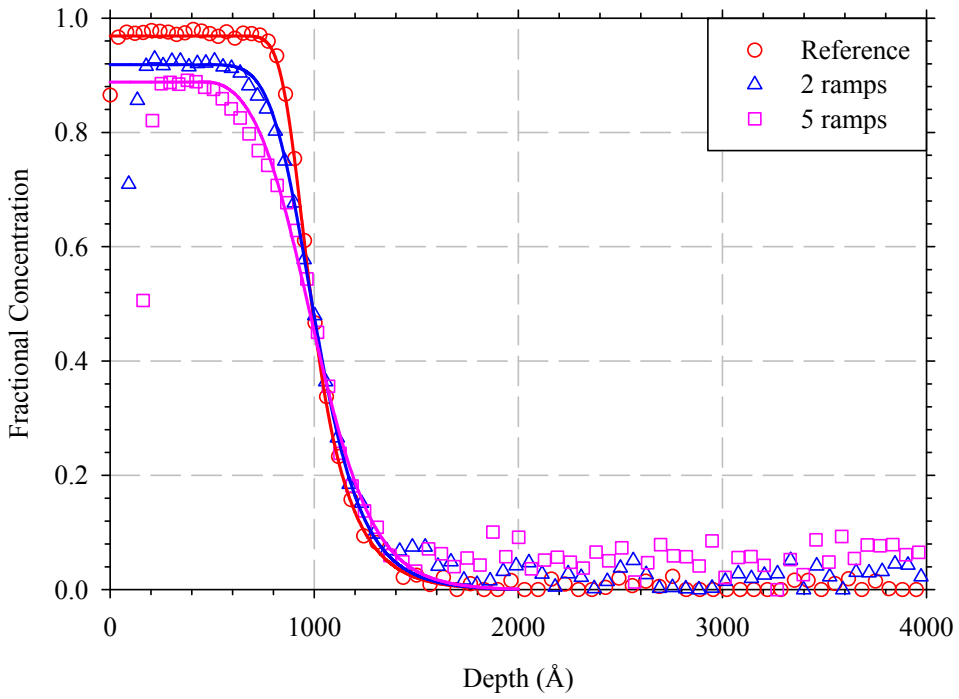

Figure 6.6: Example of linearly ramped data and MRI fits, ramped to a maximum temperature of 400 ^{o}C.

The linear temperature ramp profiles used in this study are shown in Figure 6.7. From Figure 6.7 it can be seen that two temperature ramping profiles, namely 375 ^{o}C and 450 ^{o}C, deviated from the programmed heating profile. This deviation influences the time used for the perfect classical analysis technique and warrants further investigation.

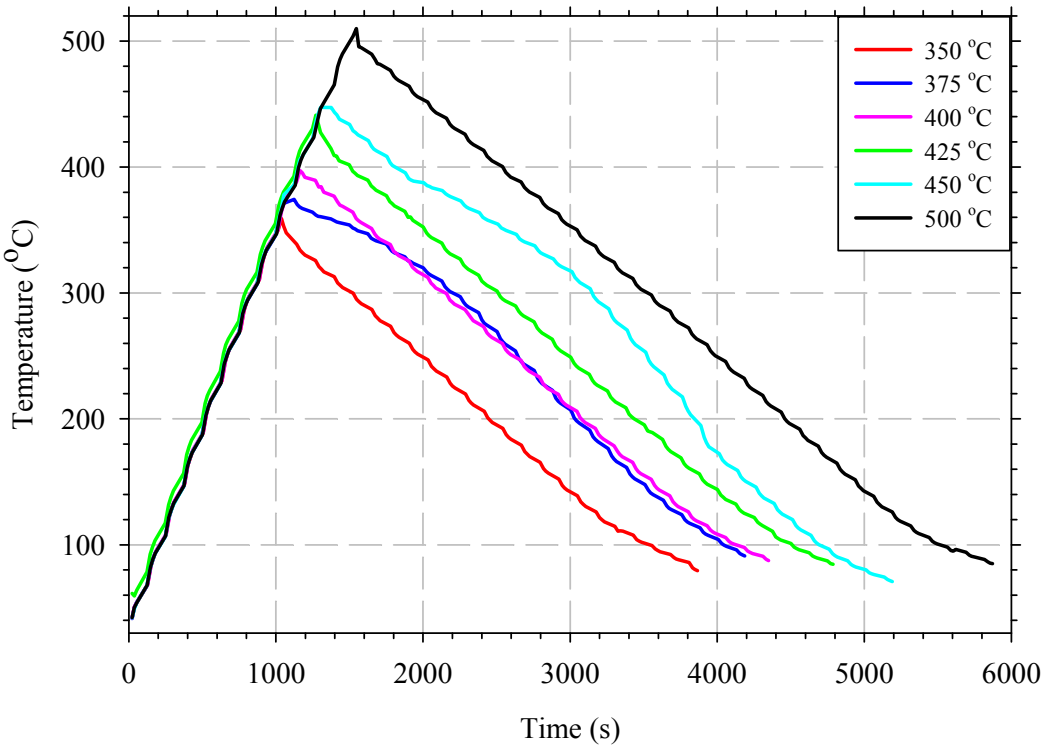

Figure 6.7: Linear ramping temperature profiles used in this study. A deviation from the ideal linear temperature ramp is visible for the measured temperature ramping profiles of 375 °C and 450 °C.

Since the profiles are quantified, one can fit a polynomial function through each of the temperature ramping profiles which allows accurate calculation of the temperature at a particular point in time. Using the polynomial function, the perfect classical annealing time can then be obtained as described in Chapter 4.

Once again, the MRI model was used and the surface roughness parameter was determined for the linearly ramped samples. The MRI parameters for linear ramping are listed in Table 6.3 from which $\Delta\sigma^2$ vs. time graphs were constructed, shown in Figure 6.8 and Figure 6.9.

Sample nr	Ramps	w(λ)	σ(λ)	Ramp T (°C)
1	-	16	8	-
1	1		9	350
1	2		10	
1	3		11	
8	4		12.5	
8	5		13	
2	-	16	8	-
2	1		30	500
2	2		38	
2	3		48	
3, 4	-	16	7	-
3	1		11	400
3	2		13	
4	3		15	
4	4		17.5	
4	5		19	
6	-	16	7	-
6	3		11.5	375
6	6		15	
6	9		17	
6	2		10.5	
6	4		12.5	
7	-	16	4	-
7	1		15	450
7	2		18.5	
7	3		23	

Table 6.3: Best fit surface roughness and mixing width obtained for the different linearly ramped samples

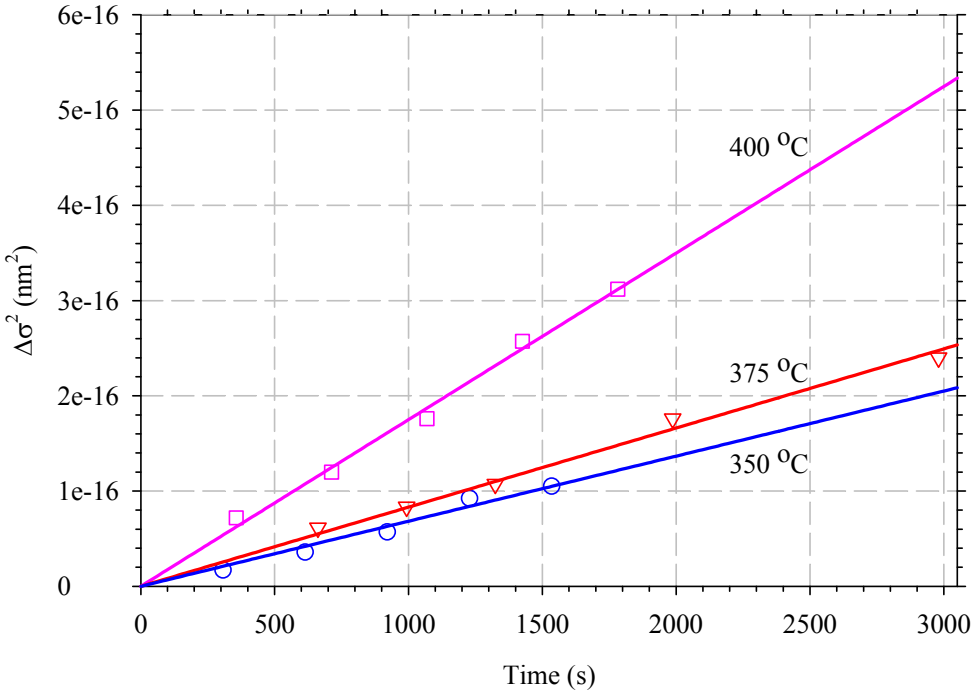

Figure 6.8: Best fit MRI parameters for the samples linearly ramped to 350 °C, 375 °C and 400 °C.

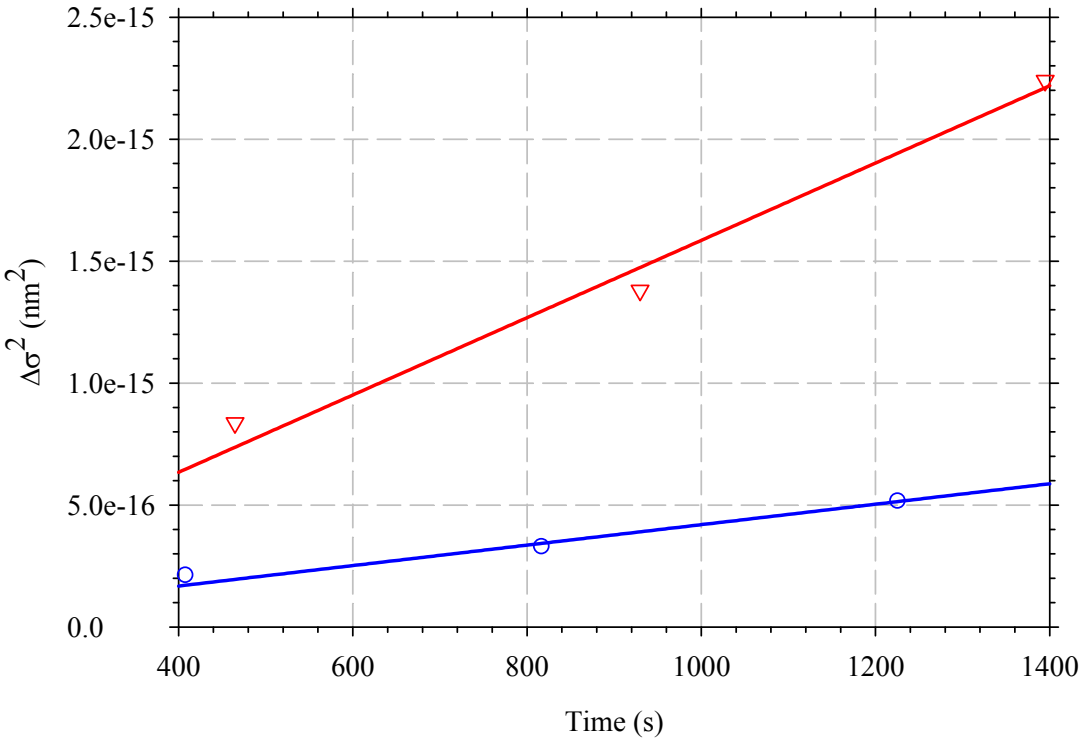

Figure 6.9: Best fit MRI parameters for the samples linearly ramped to 450 °C and 500 °C.

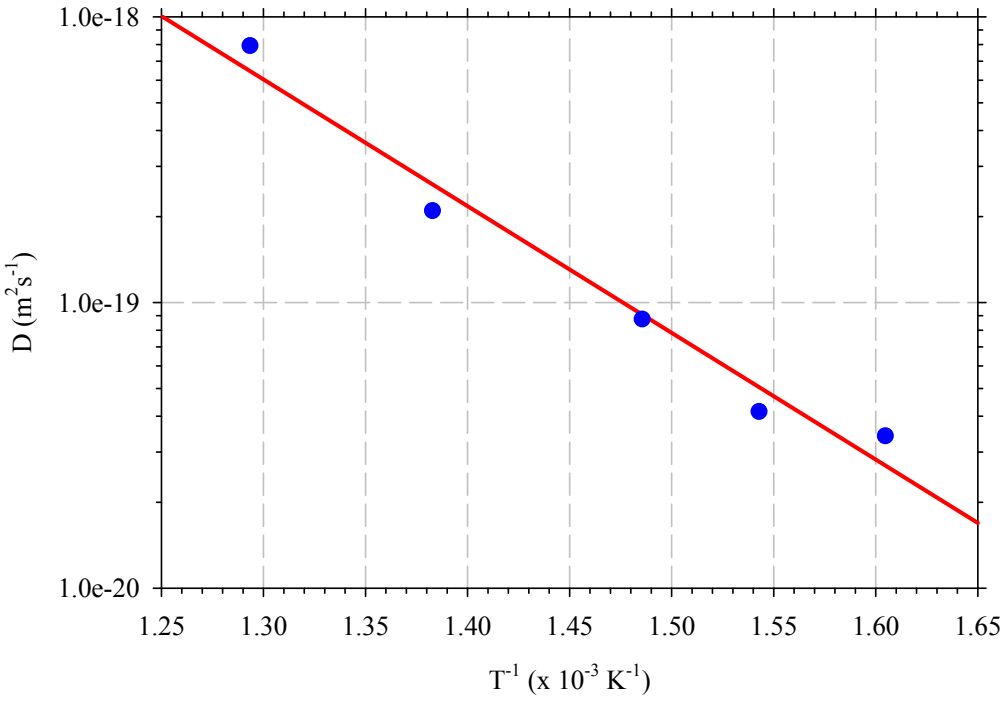

Figure 6.10: Arrhenius graph constructed from the MRI parameters for linear ramping.

Source	D_0 $\left(\mathrm{m^2.s^{-1}}\right)$	Q $\left(\mathrm{kJ.mol^{-1}}\right)$
Linear Ramping	4.76×10^{-13}	85.4
Classical Annealing	6.48×10^{-9}	130.5
Ref. [54]	2×10^{-5}	228.7
Ref. [55]	2.6×10^{-10}	133.1
Ref. [56]	6.93×10^{-7}	90.4
Ref. [57]	1.4×10^{-14}	106.1
Ref. [58]	4.9×10^{-13}	103.2

Table 6.4: Diffusion parameters obtained in the present work and from literature.

From Figure 6.8 and Figure 6.9, an Arrhenius graph was constructed and is shown in Figure 6.10. Linear regression was applied to Figure 6.10 and the diffusion parameters, obtained by the same method discussed in the previous section, are listed in Table 6.4.

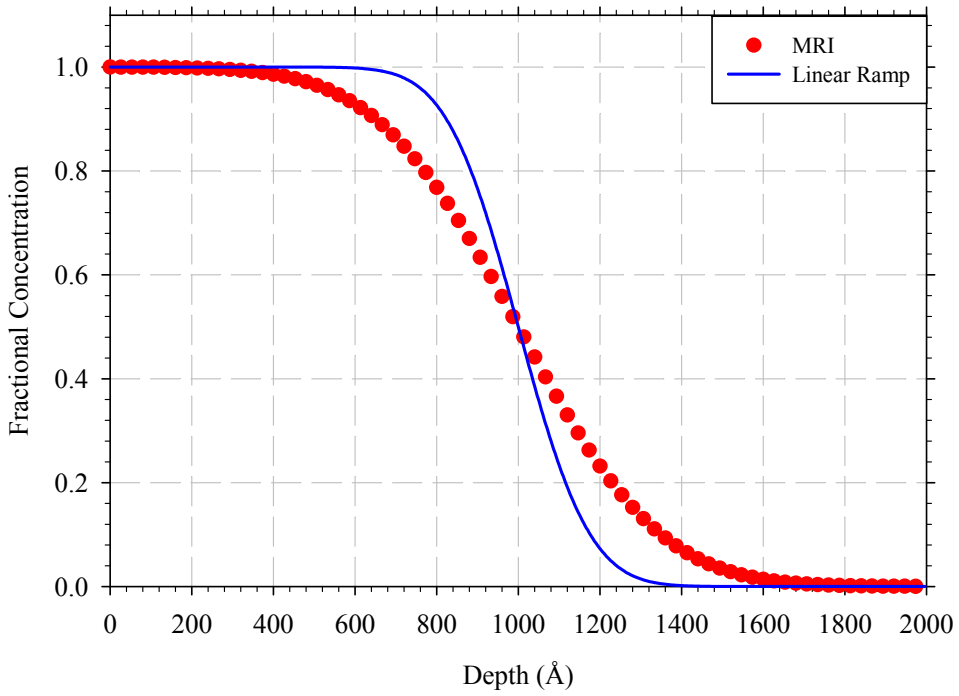

Figure 6.11: Comparison of calculated classical and linear ramping diffusion profiles. The calculation was performed with the diffusion parameters obtained from the classical heating analysis and the linear ramping analysis.

The diffusion parameters obtained from linear ramping are significantly smaller than the diffusion parameters obtained by applying the MRI model to a classical heat treatment. This implies that the classical analysis yielded diffusion parameters that over-estimated the rate of diffusion. A comparison between a diffusion profile calculated with classical and linear ramp diffusion parameters is shown in Figure 6.11 to illustrate this point. The diffusion profile calculated using classically obtained diffusion parameters predicts more diffusion than the linearly ramped profile.

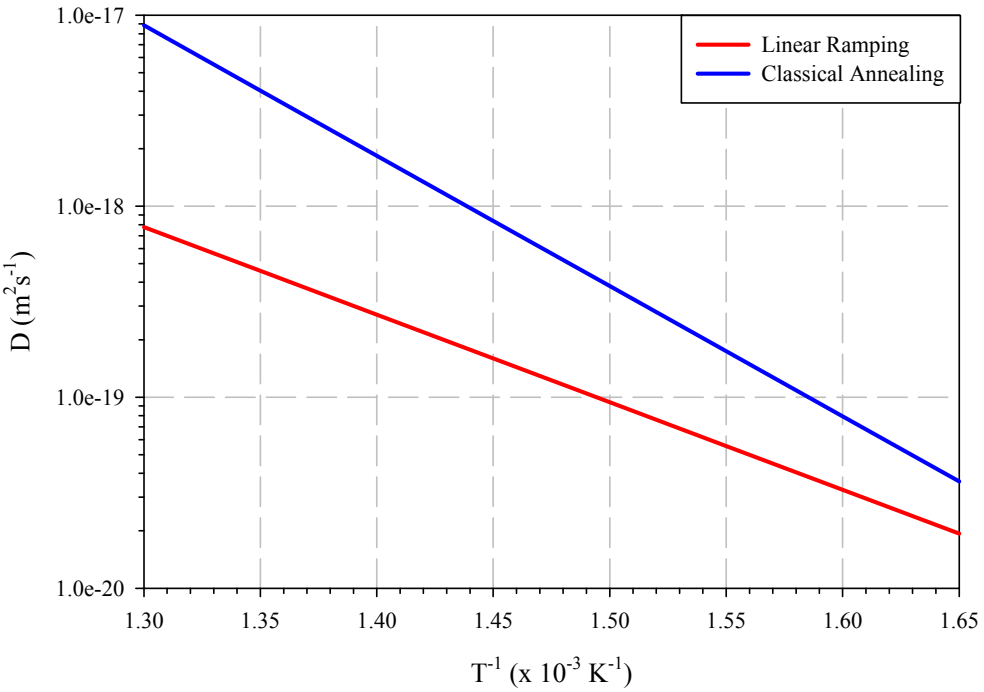

Figure 6.12: Comparison of Arrhenius graphs for classical heating method and linear ramping.

A further comparison of the Arrhenius graphs of classical heating and linear ramping, shown in Figure 6.12, also illustrates this point. This correlates well to the results obtained in [60], highlighting the importance of controlling the heat treatment that is used during diffusion studies.

One advantage of using controlled linear ramping is the ability to change the rate at which a sample is heated. Increasing or decreasing the heating rate and/or the cooling rate allows one to probe higher or lower temperatures as well as shorter annealing times for fast diffusing species. The next section illustrates the effect of increasing the heating rate and the results obtained from the increased heating rate.

6.4 Diffusion Coefficient of Ni in Cu – Linearly Ramped Heating: Extending the technique

The maximum temperature used for linear ramping in the previous section resulted in depth profiles that were a challenge to fit with the MRI model. This means that the maximum temperature limit for the linear ramping heating and cooling rate was reached at 500 ^{o}C. If measurements are required beyond 500 ^{o}C, the annealing time must be shortened; else the diffusion profile will become unusable. This can be achieved by increasing either the heating rate or the cooling rate, or both. If one now assumes that the diffusion mechanism that governs diffusion over the measured temperature ranges is the same, then changing the heating rate will allow probing into higher temperatures than what is possible for classical annealing. This is already evident in the difference between the maximum temperature (350 ^{o}C) reached for the classical annealing and the maximum for linear heating (500 ^{o}C).

For the purposes of this part of the study, two variations of the linear ramping profile were used. For the first variation, only the heating rate was increased to 1 $^{\circ}C.s^{-1}$ while the cooling rate was kept at 0.1 $^{\circ}C.s^{-1}$. This change results in a reduced effective annealing time when compared to the previous annealing time for 400 ^{o}C, shown in Figure 6.13. Since the effective annealing time is lower, a temperature of 550 ^{o}C was selected as the maximum ramping temperature for the higher heating rate part of the study.

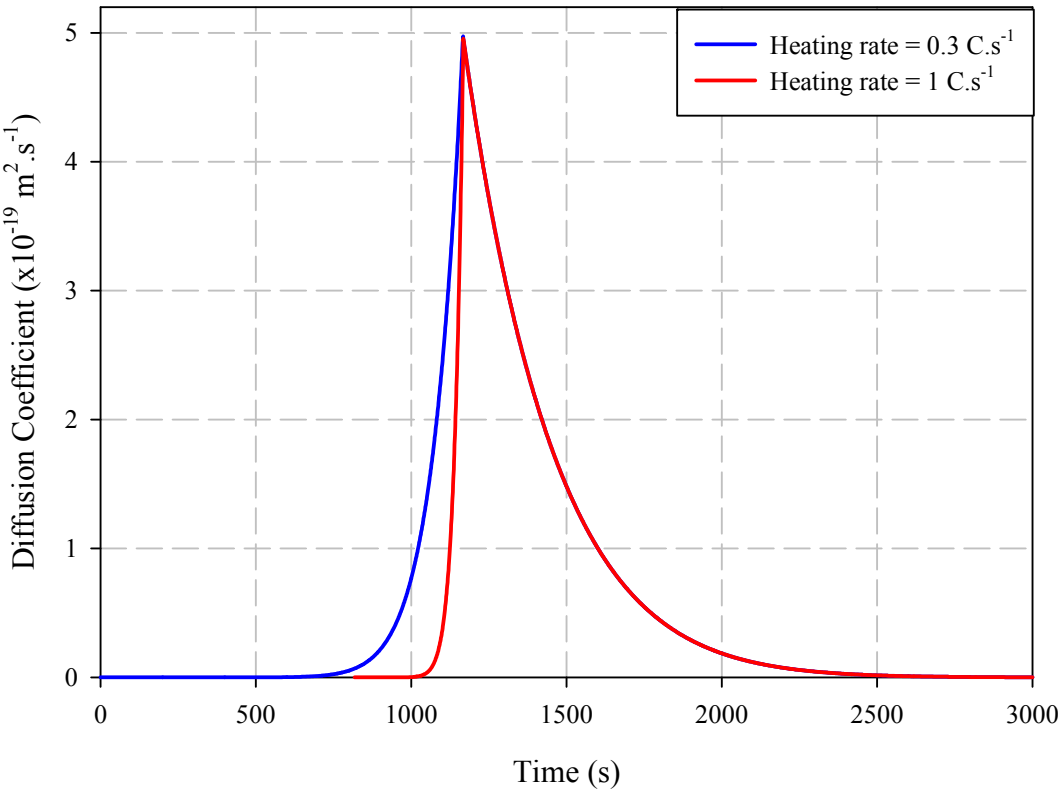

Figure 6.13: Illustration of the effect that changing the heating rate from 0.3 $^{\circ}C.s^{-1}$ to 1 $^{\circ}C.s^{-1}$ has on the diffusion coefficient as it changes with time, ramped to a maximum temperature of 400 ^{o}C.

The second variation involved changing the heating and cooling rate to 0.6 $^{\circ}C.s^{-1}$ and -0.2 $^{\circ}C.s^{-1}$ and applying these heating and cooling rates to a maximum temperature of 450 ^{o}C. This temperature was chosen because this temperature was used in the previous section as well. The purpose of the second variation on the linear ramping method is to determine if depth profiles obtained for a constant temperature, but varying heating and cooling rates, can be compared to one another.

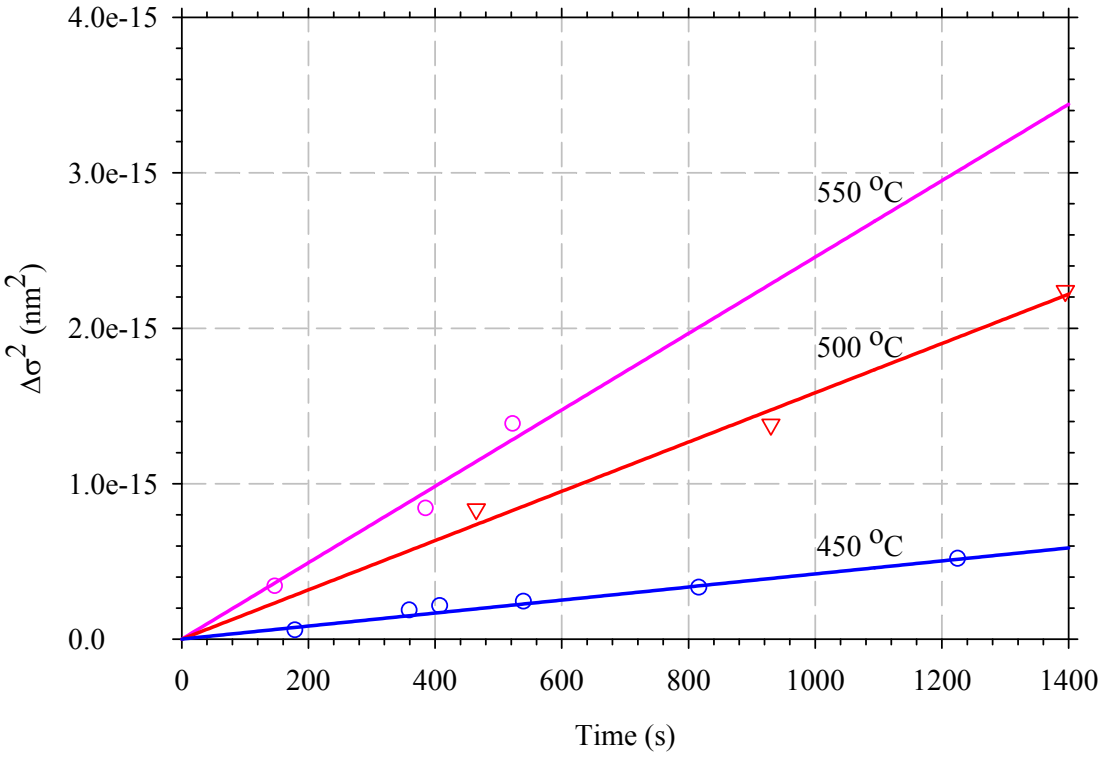

Figure 6.14: Best fit MRI parameters for the diffusion profile obtained for the two variations discussed in the text.

Stated differently, the diffusion distances obtained for this part of the experiment should overlap with the distances obtained for the same temperature but with a heating and cooling rate of 0.3 $^{\circ}C.s^{-1}$ and -0.1 $^{\circ}C.s^{-1}$.

Both of the variations mentioned in the previous paragraphs should increase the accuracy of the diffusion parameters obtained for linear ramping.

The MRI results are shown in Figure 6.14 and the Arrhenius graph resulting from the MRI fit is shown in Figure 6.15.

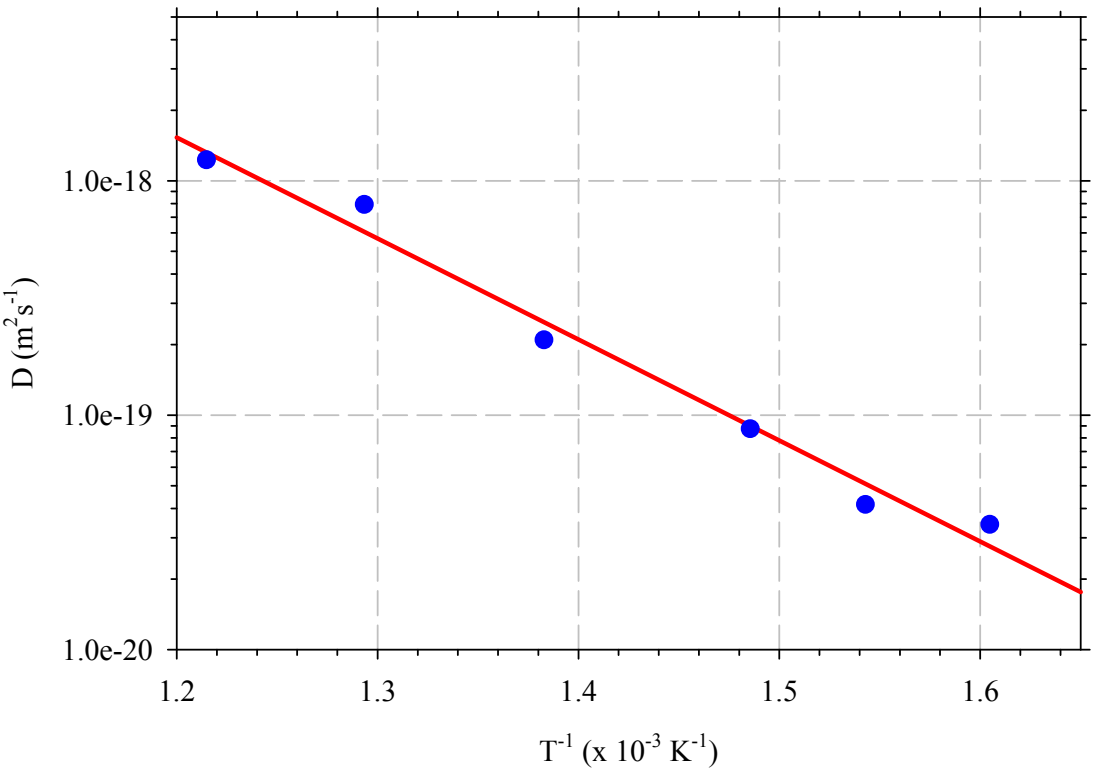

Figure 6.15: Arrhenius graph showing the extra point derived from increasing the linear ramping heating rate.

As is evident from Figure 6.15, the higher temperature result follows the results obtained in the previous section, indicating that the increased rate of heating allowed a much higher temperature to be reached than would normally be possible.

The extra point on the Arrhenius graph (Figure 6.15) also refines the diffusion parameters obtained from linear ramping even further, with a slight change in the frequency factor and the activation energy, listed in Table 6.5.

Also, the three extra points for the 450 ^{o}C line follows the previous linear ramping results closely, further refining the diffusion parameters.

Source	D_0 $\left(\mathrm{m^2.s^{-1}}\right)$	Q $\left(\mathrm{kJ.mol^{-1}}\right)$
Linear Ramping – higher temperature and heating/cooling rate	2.29×10^{-13}	82.5
Linear Ramping	4.76×10^{-13}	85.4
Classical Annealing	6.48×10^{-9}	130.5
Ref. [54]	2×10^{-5}	228.7
Ref. [55]	2.6×10^{-10}	133.1
Ref. [56]	6.93×10^{-7}	90.4
Ref. [57]	1.4×10^{-14}	106.1
Ref. [58]	4.9×10^{-13}	103.2

Table 6.5: Comparison of diffusion parameters obtained from classical annealing, literature and varying the heating rate of the linear ramp anneal.

The diffusion parameters obtained from the linear ramping approach are significantly smaller than the diffusion parameters obtained by applying the MRI model to a classical heat treatment. This implies that the classical analysis yielded diffusion parameters that over-estimated the rate of diffusion. This correlates well to the results obtained in [60], highlighting the importance of controlling the heat treatment that is used during diffusion studies.

Chapter 7 – Conclusion

The purpose of this study was to determine the effect that the annealing method has on the diffusion parameters extracted from depth profiles. As a precursor to the experimental study, a thorough investigation of diffusion and the various factors that contribute to diffusion was conducted. Next, the effect of the annealing method was analysed by measuring an actual annealing profile taken in atmosphere. From the measured heating profile, the emissivity of a stainless steel sample was determined and a calculation yielded the heating profile of the stainless sample in a vacuum. The heating profile indicated that a considerable amount of time was needed before the sample reached the annealing temperature and similarly, the sample took a long time to cool down to room temperature. This implies that a sample annealed in vacuum conditions will not necessarily reach the annealing temperature for short annealing times.

The aforementioned raised an important question as to how one can determine the diffusion parameters of fast diffusing species. If one employs a classical annealing method, the annealing temperature must be reduced significantly, or the measured depth profile will be very difficult to analyse. Also, since the annealing takes place in an uncontrolled fashion, the diffusion parameters obtained from such diffusion studies are questionable. In order to eliminate the question of annealing method, a controlled linear ramp heating method was proposed. The study consisted of two parts, a classical diffusion analysis and a linear ramping diffusion analysis.

For the classical diffusion analysis, experimentally prepared Cu/Ni thin films were analyzed by means of ion erosion Auger electron spectroscopy. The MRI model was successfully employed to reconstruct the experimental profiles and using the surface roughness parameter the diffusion coefficient for nickel in copper was found to be $D_0 = 6.49 \times 10^{-9}$ $m^2.s^{-1}$ and $Q = 130.5$ $kJ.mol^{-1}$. These values are considerably smaller than the coefficients determined from single crystal diffusion studies at higher temperatures, e.g. $Q = 258$ $kJ.mol^{-1}$ [61]. The results indicate a different process of diffusion than vacancy diffusion prevailed in this study. Previous research [56] determined that the most important diffusion mechanism responsible for diffusion at low-temperatures for polycrystalline Cu/Ni was grain boundary diffusion and the results obtained in this part of the study support this. The results obtained also compare well to diffusion parameters obtained by other research groups.

The second part of the study involved samples that were subjected to a controlled heat treatment in an ultra high vacuum environment. To analyse the samples that underwent linear ramping, a perfect classical heat treatment was proposed. The MRI model, in conjunction with the proposed perfect classical heating method, was used to determine the diffusion parameters of Ni in Cu, with values of $D_0 = 2.29 \times 10^{-13}$ $m^2.s^{-1}$ and $Q = 82.5$ $kJ.mol^{-1}$. These parameters are smaller than the parameters obtained from classical annealing which indicate an over-estimation of diffusion when using the classical heat treatment.

Since the preparation conditions of the samples analysed (linearly ramped and classically annealed) are the same, only the annealing method will result in different diffusion parameters being extracted from the measured depth profiles. One can then

conclude that the method of annealing plays an important part when attempting to extract diffusion parameters.

Two variations on the linear ramping method were also investigated. The variations involved changing the heating and cooling rate so that a higher temperature could be probed. Furthermore, different heating and cooling rates were used for a fixed temperature. Both the aforementioned experiments followed the results of the initial linear ramping experiments. The linear ramping annealing method is therefore a versatile method with multiple variations that assists in determining diffusion parameters for thin film samples.

Chapter 8 – References

1 M Ohring, *Materials Science of Thin Films*, 2nd Edition, Academic Press: New York, 2004

2 FR Banks, *Physics Review,* 1941, **59**, 376

3 A. Fick, *Philosophical Magazine*, 1855, **10**, 30

4 R.J. Borg, G.J. Dienes, *An Introduction to Solid State Diffusion*, Boston Academic Press, 1988

5 J. du Plessis, P.E. Viljoen and G.N. van Wyk, *Surface Science*, 1991, **244**, 277

6 B. Tuck, *Introduction to diffusion in semiconductors*, IEE Monograph Series 16, Peter Peregrinus Ltd., 1974

7 D.A. Porter, K.E. Easterling, *Phase Transformations in Metals and Alloys*, Chapman & Hall, (1981)

8 H.D. Joubert, *A Monte Carlo program for simulating segregation and diffusion utilizing chemical potential calculations*, M.Sc thesis, University of the Free State, 2004

9 DR Askeland, *The Science and Engineering of* Materials, 3rd S.I. Edition, Stanley Thornes Publishers: London, 1998

10 RJ Borg, GJ Dienes, *An Introduction to Solid State Diffusion*, Boston Academic Press: London, 1988

11 PG Shewmon, *Diffusion in Solids*, McGraw-Hill Book Company: New York, 1963

12 ME Glicksman, *Diffusion in Solid - Field Theory, Solid-State Principles and Applications*, 1st edition. John Wiley: Chichester, 2000

13 MA Omar, *Elementary solid state physics: principles and applications*, 1st edition, Addison-Wesley: London, 1975

14 B Tuck, *Introduction to Diffusion in Semiconductors*, IEE Monograph Series 16, Peter Peregrinus Ltd.: Stevenage, England, 1974

15 K Huang, *Introduction to Statistical Physics*, Taylor & Francis Ltd: London, 2001

16 TW Dobson, JF Wager, JA Van Vechten, *Physics Review*, *B*, 1989, **35 No 5**, 2962

17 FW Sears, GL Salinger, *Thermodynamics, Kinetic Theory, and Statistical Thermodynamics*, Addison-Wesley Publishing Company: London, 1986

18 HB Huntington, GA Shirn, ES Wajda, *Physics Review*, 1955, **99,** 1085

19 P Wynblatt, *Journal of Physics and Chemistry of Solids*, 1969, **30**, 2201

20 JJ Burton, *Physics Review B*, 1972, **5**, 2948

21 JA Van Vechten, *Physics Review B*, 1976, **12**, 1247

22 JA Van Vechten, JF Wager, *Physics Review B*, 1985, **32**, 5259

23 JF Lee, FW Sears, DL Turcott, *Statistical Thermodynamics,* 2nd edition, Addison-Wesley: Reading, Massachusetts, 1972

24 L Dobrzynski, *Journal of Physics and Chemistry of Solids*, 1969, **30**, 2395

25 CP Flynn, *Physics Review*, 1968, **171**, 682

26 JJ Terblans, WJ Erasmus, EC Viljoen, J du Plessis, *Surface and Interface Analysis* 1999, **28**, 70.

27 JJ Terblans, *Surface and Interface Analysis*, 2002; **33**, 767

28 RC Weast, MJ Astle, *CRC Handbook of Chemistry and Physi*cs, 63rd edition, CRC Press, Inc., 1982: F52

29 F Seitz, *Acta Crystallographica*, 1950, **3**, 355

30 A Vignes, *Industrial and Engineering Chemistry Fundamentals*, 1966, **5**, 189

31 LS Darken, *Transactions of the American Institute of Mining and Metallurgical Engineers*, 1948, **175**, 184

32 J Crank, *The Mathematics of Diffusion*, Oxford University Press, 1975

33 RL Burden and JD Faires, *Numerical Analysis*, 6th Edition, Brooks/Cole Publishing Company: New York, 1997

34 DR Vij, *Handbook of Applied Solid State Spectroscopy*, Springer US, 2006

35 S Hofmann, *Reports on Progress in Physics*, 1998, **61**, 827

36 S Hofmann *Surface and Interface Analysis*, 1994, **21**, 673

37 S Hofmann, *Surface and Interface Analysis*, 2000, **30**, 228

38 J.Y. Wang, S. Hofmann, A. Zalar, E.J. Mittemeijer, *Thin Solid Films,* 2003, **444,** 120

39 P. Süle, L. Kotis, L. Toth, M. Menyhard, W.F. Egelhoff Jr.*, Nuclear Instruments and Methods B,* 2008, **266**, 904

40 S. Hofmann, *Thin Solid Films,* 2001, **336**, 398

41 T. Wöhner, G. Ecke, H. Rößller, S. Hofmann, *Fresenius' Journal of Analytical Chemistry*, 1995, **353**, 447

42 JY Wang and EJ Mittemeijer, *Journal of Materials Research*., 2004, **19**, 3389

43 D Halliday, R Resnick and J Walker, *Fundamentals of Physics, Extended*, John Wiley and Sons, Inc.: New York, 1997

44 AS Dobrosavljević and KD Maglić, *International Journal of Thermophysics*, 1992, **13**, 57

45 CT O'Sullivan, *American Journal of Physics*, 1990, **58**, 956

46 JH Mathews, *Numerical Methods for Mathematics, Science and Engineering*, Prentice-Hall International, Inc., London, 1992

47 W. A. Pliskin, E. E. Conrad, *I.B.M Journal*, January 1964

48 W.D. Roos, G.N. van Wyk and J. du Plessis, *Surface and Interface Analysis*, 1994, **22**, 65

49 P.W. Palmberg, *Analytical Chemistry*, 1973, **45**, 549A

50 S. Hofmann, *Vacuum*, 2009, **48 Number 7-9**, 607

51 G.C. Smith, *Compositional Analysis by Auger Electron And X-ray Photoelectron Spectroscopy*, in Handbook of surface and interface analysis: methods for problem-solving 2nd ed., (J.C. Rivière and S. Myhra, eds.), Marcel Dekker Inc., New York, 1998, chap. 5 pp 159

52 M.P. Seah, *Quantification of AES and XPS*, in Practical Surface Analysis, 2nd ed., Vol. 1, Auger and Photoelectron Spectroscopy (D. Briggs and M.P. Seag, eds.), Wiley, Chichester, 1990, chap. 5, pp 201

53 R. Shimizu, *Japanese Journal of Applied Physics*, 1983, **22**, 1631

54 T. Vandijk, E. J. Mittemeijer, *Thin Solid Films*, 1977**, 41**, 173

55 B. C. Johnson, C. L. Bauer, A. G. Jordan, *Journal of Applied Physics*, 1986, **59**, 1147

56 S. Divinski, J. Ribbe, G. Schmitz, C. Herzig, *Acta Materialia*, 2007, **55**, 3337

57 R. Venos, W. Pamler, H. Hoffmann, *Thin Solid Films*, 1988, **162**, 155

58 N. N. Rammo, M. N. Makadsi, A.M. Abdul-Letiff, *Physica Status Solidi (A)*, 2004, **201 No. 14**, 3102

59 R. W. Bauer, A. M. Schwartzman, C. D. Antonio, *Thin Solid Films*, 1968, **2**, 529

60 H.D. Joubert, J.J. Terblans, H.C. Swart, *Nuclear Instruments and Methods B*, 2009, **267**, 2575

61 R.C. Weast, M.J. Astle, W.H. Beyer, *CRC Handbook of Chemistry and Physics, 65th edition*, CRC Press, Inc., Boca Raton Florida, **1984.**

Chapter 9 – Conference Contributions and Published Articles

9.1 Publications

Extracting inter-diffusion parameters from Ni/Cu thin films by means of profile reconstruction with the MRI model, HD Joubert, JJ Terblans, HC Swart.

Surface and Interface analysis, Volume 42, Page 1281, 2010

Determining the diffusion coefficient of Ni in Cu from a Ni/cu thin film using linear heating, scanning Auger microscopy and a numerical solution of Fick's second Law, HD Joubert, JJ Terblans, HC Swart.

Surface and Interface Analysis, Volume 42, Page 1213, 2010

Comparison of inter-diffusion coefficients for Ni/Cu thin films determined from classical heating analysis and linear temperature ramping analysis by means of profile reconstruction and a numerical solution of Fick's law, HD Joubert, JJ Terblans, HC Swart.

Nuclear Instruments and Methods B, Volume 267, Issue 16, Page 2575, 2009

Effect of slow heating and -cooling on the interdiffusion of thin films, HD Joubert, JJ Terblans, HC Swart.

Surface Review and Letters, Volume 14, Issue 4, Page 703, 2007

9.2 Conference contributions

Extracting inter-diffusion parameters from Ni/Cu thin films by means of profile reconstruction with the MRI model, HD Joubert, JJ Terblans, HC Swart.
Poster presented at the 13th European Conference on Applications of Surface and Interface Analysis, Antalya, Turkey, 18 to 23 October 2009

Determining the diffusion coefficient of Ni in Cu from a Ni/cu thin film using linear heating, scanning Auger microscopy and a numerical solution of Fick's second Law, HD Joubert, JJ Terblans, HC Swart.
*Poster presented at the 13th European Conference on Applications of Surface and Interface Analysis, A*ntalya, Turkey, 18 to 23 October 2009

Comparison of inter-diffusion coefficients for Ni/Cu thin films determined from classical heating analysis and linear temperature ramping analysis by means of profile reconstruction and a numerical solution of Fick's law, HD Joubert, JJ Terblans, HC Swart.
Poster presented at the 23rd International Conference on Atomic Collisions in Solids, Hans Merensky Golf Estate, Phalaborwa, South Africa, 16 to 22 August 2008

Extracting inter-diffusion parameters from Ni/Cu thin films by means of profile reconstruction with the MRI model, HD Joubert, JJ Terblans, HC Swart.
Poster presented at the 23rd International Conference on Atomic Collisions in Solids, Hans Merensky Golf Estate, Phalaborwa, South Africa, 16 to 22 August 2008

The use of a modified heating method to investigate the Cu/Ni interdiffusion parameters, HD Joubert, JJ Terblans, HC Swart.

Poster presented at the 53rd conference of the South African Institute of Physics

University of Limpopo, Turfloop Campus, Polokwane, South Africa, 2008

Effect of slow heating and -cooling on the interdiffusion of thin films, HD Joubert, JJ Terblans, HC Swart.

Poster presented at the Asian Pacific Conference on Surface Science and Engineering, Hong Kong, People's Republic of China, 18 to 20 December, 2006

Appendix A – Visual basic source code for MRI analysis software

```
Option Explicit

'experimental data
Public xData() As Single, CuData() As Single, NiData() As
     Single
Public OData() As Single, CData() As Single, SiData() As
     Single

'generated data of original as deposited sample
Public xOrig() As Single, CuOrig() As Single, NiOrig() As
     Single
'working arrays
Public CuWork() As Single, NiWork() As Single

'settings for original profile generation
Type ProfileSettings
  ConcL1 As Single
  ConcL2 As Single
  HHPosition As Single
  EndPosition As Single
  Resolution As Single
End Type
Public ProfSet As ProfileSettings
'tells program what type of mixing to perform, 1 for
     average,2 for linear, etc.
Public method As Integer
'mixing width
Public MixWidth As Single
'info depth
Public infdepth As Single
'roughness
Public SurRough As Single


Public Sub MixingRoutine(ByRef Graph As EZGraph)

  'first fill the mixing arrays
  Call Fill_Arrays

  'decide what type of mixing to do
  Select Case method

    Case 1 'average
```

```
      Call Average_Mixing
      Call InfoDepth
      Call SurfaceRoughness

    Case 2 'linear

      Call Linear_Mixing

    Case 3 'exponential

      Call Exponential_Mixing
      Call SurfaceRoughness

    Case 4 'mri

      Call AtomicMixing
      Call InfoDepth
      Call SurfaceRoughness

  End Select

  Graph.LineGraphArray 3, xOrig(), NiWork(), RGB(255, 0,
     255), 1, UBound(xOrig()), "Ni Recon"
  Graph.XAxisMaximum = 2000
  MsgBox "Calculation complete.", vbOKOnly

End Sub

Private Sub Average_Mixing()

  Dim i As Long, j As Long
  Dim lWidth As Long 'width of mixingzone ito array
     indeces
  Dim Favg As Single 'average value used in mixing the
     layers

  'first find the width of the mixing zone ito array
     indeces
  lWidth = MixWidth / ProfSet.Resolution

  'For   i   =   0   To   UBound(NiWork())   -   lWidth
     'UBound(xOrig()) - lWidth
 For  i  =  ProfSet.HHPosition  /  ProfSet.Resolution  -
     MixWidth / ProfSet.Resolution To UBound(NiWork()) -
     MixWidth / ProfSet.Resolution
    DoEvents
    'reset the averaging variable
    Favg = 0

    For j = 0 To lWidth - 1
```

```
      Favg = Favg + NiWork(i + j) 'at position i, start
     by adding the layers from i to the width lWidth,then
     increment the position in the array and repeat
    Next

    If NiWork(i + j) <> 1 Then
      Debug.Print
    End If
    'find the average
    Favg = Favg / lWidth

    'now fill the mixing area with the average
    For j = 0 To lWidth - 1
      NiWork(i + j) = Favg
    Next

  Next

End Sub

Private Sub Linear_Mixing()
  Dim i As Long, j As Long
  Dim lWidth As Long 'width of mixingzone ito array
     indeces
  Dim M As Single 'gradient of straight line
  Dim c As Single

  'first find the width of the mixing zone ito array
     indeces
  lWidth = MixWidth / ProfSet.Resolution

  For i = 0 To UBound(xOrig()) - lWidth

    DoEvents

    If xOrig(i) >= 999.5 Then
    Debug.Print
    End If

    M = 0

    M = (NiWork(i + lWidth) - NiWork(i)) / lWidth
    c = NiWork(i)


    For j = 0 To lWidth - 1
      NiWork(i + j) = M * (j) + c 'at position i,
     calculate the new concentration,then increment the
     position in the array and repeat
    Next
```

```
  Next

End Sub

Private Sub Exponential_Mixing()
  Dim i As Long
  Dim x As Single 'concentration of the second layer, see
     thesis for information

  If MixWidth = 0 Then Exit Sub

  'loop throug from HHposition - mixing width to second
     interface - width
  'transform the position info to array index info
  For  i  =  ProfSet.HHPosition  /  ProfSet.Resolution  -
     MixWidth / ProfSet.Resolution To UBound(NiWork()) -
     MixWidth / ProfSet.Resolution

    'use the second layer's concentration to determine
     the concentration of the second layer after mixing
    'see thesis for more info.  (transformation of i from
     array index to depth takes place here)

    x = x * (Exp(-MixWidth))

    'now calculate the concentration of the first layer
    NiWork(i) = (x)  '* ProfSet.Resolution


    DoEvents

  Next
End Sub

Private Sub Fill_Arrays()
  Dim i As Long

  'size the arrays according to the resolution
  ReDim NiWork(ProfSet.EndPosition / ProfSet.Resolution)
  ReDim CuWork(ProfSet.EndPosition / ProfSet.Resolution)

  For i = 0 To UBound(NiOrig())
    NiWork(i) = NiOrig(i): CuWork(i) = CuOrig(i)
  Next

End Sub

Private Sub AtomicMixing()

  Dim i As Long
```

```
  Dim x As Single 'concentration of the second layer, see
     thesis for information

  If MixWidth = 0 Then Exit Sub

  'loop throug from HHposition - mixing width to second
     interface - width
  'transform the position info to array index info
  For  i  =  ProfSet.HHPosition  /  ProfSet.Resolution  -
     MixWidth / ProfSet.Resolution To UBound(NiWork()) -
     MixWidth / ProfSet.Resolution

    'use  the  second  layer's  concentration  to  determine
     the concentration of the second layer after mixing
    'see thesis for more info.  (transformation of i from
     array index to depth takes place here)
    x  =  1  *  (1  -  Exp(-(i  *  ProfSet.Resolution  -  0  +
     MixWidth) / MixWidth))

    x   =   x   *   (Exp(-(i   *   ProfSet.Resolution   -
     ProfSet.HHPosition + MixWidth) / MixWidth))

    'now calculate the concentration of the first layer
    NiWork(i) = (x)  '* ProfSet.Resolution

    DoEvents

  Next

End Sub

Private Sub InfoDepth()

  Dim i As Long
  Dim x As Single 'concentration of the second layer, see
     thesis for information

  'loop throug from HHposition - mixing width to second
     interface - width
  'transform the position info to array index info

  If infdepth = 0 Then Exit Sub

  For  i  =  ProfSet.HHPosition  /  ProfSet.Resolution  -
     MixWidth / ProfSet.Resolution To UBound(NiWork())
  On Error Resume Next

    x  =  (NiWork(i))  *  (1  -  Exp(-(MixWidth  /  infdepth)))
     '+ Exp(-MixWidth / infdepth) * _
                  (1  -  Exp(-(ProfSet.EndPosition  -  i  *
     ProfSet.Resolution - MixWidth) / infdepth))
```

```
    'now calculate the concentration of the first layer
    NiWork(i) = x '* ProfSet.Resolution
    'Debug.Print (1 - X)

    DoEvents

  Next

End Sub

Public Sub SurfaceRoughness()
On Error Resume Next

Dim M As Integer
'contribution from the surface roughness

Dim Favg As Single
'Dim length As Integer: length = UBound(NiWork())
Dim NiTemp(20000) As Single
Dim i As Single

     For    i    =    0    To    ProfSet.EndPosition    /
     ProfSet.Resolution
        DoEvents
        If SurRough = 0 Then          'In this case, the
     contribution from surface roughness is ignored
          Exit Sub
          'Cf(i) = Ci(i)

        ElseIf   i   >=   SurRough   Then   'ElseIf   i   *
     ProfSet.Resolution - ProfSet.Resolution >= SurRough
     Then

            For M = 0 To i 'Int(i + 3 * SurRough /
     ProfSet.Resolution - ProfSet.Resolution)
              NiTemp(i)   =   NiTemp(i)   +   NiWork(M)   /
     (SurRough * Sqr(2 * 3.14159)) * Exp(-((i - M) *
     ProfSet.Resolution) ^ 2 / (2 * SurRough ^ 2))
            Next M

            NiTemp(i) = NiTemp(i) * ProfSet.Resolution

        Else
            NiTemp(i) = NiWork(i)

        End If

     Next i
```

```
      For    i    =    0    To    ProfSet.EndPosition    /
      ProfSet.Resolution
         NiWork(i) = NiTemp(i)
      Next

End Sub
```